Calculation of Rydberg energy levels of rubidium in an electric field

Kalasuwan, Pruet

Calculation of Rydberg energy levels of rubidium in an electric field

Pruet Kalasuwan

A thesis submitted in partial fulfilment
of the requirements for the degree of
Master of Science

Supervisors : Prof. C.S. Adams and Dr. R.M. Potvliege

Durham University

Department of Physics
Durham University
January 10, 2008

Calculation of Rubidium Rydberg states in an Electric field

Pruet Kalasuwan

Abstract

Energy levels of Rydberg Rubidium atoms in an external electric field are calculated by Hamiltonian-diagonalization and Coulomb approximation. The results are in agreement with previous studies and with the expected scaling laws. Comparing to electromagnetically induced transparency(EIT) experiments of Rubidium vapour in 90 MHz rf electric field and room temperature of Durham University, we can observe the effect of the presence of ions and oscillating electric field. The EIT experimental results also show larger effective field than theoretical results by a factor of 1.35.

Declaration

I confirm that no part of the material offered has previously been submitted by myself for a degree in this or any other University. Where material has been generated through joint work, the work of others has been indicated.

Pruet Kalasuwan
Durham, January 10, 2008

Contents

List of Figures

List of Tables

Chapter 1

Introduction

1.1 Why this work?

The label Rydberg refers to atoms which are excited to a high principal quantum number n. In the case of alkali atoms, the orbital radius of the valence electron is correspondingly large and loosely bound. This makes Rydberg atoms have some unique properties like high sensitivity to external electric fields. Together with development in laser cooling, there are several possible mechanisms where Rydberg atoms in electric field could be introduced into quantum information processing (QIP). One of those is transferring quantum information between Rydberg atoms. It was proposed by Mourachko et al.[1] and Anderson et al.[2] that Rydberg atoms in a constant electric field can transfer their excitations to adjacent atoms if atoms are excited into energy levels that corresponds to energy transfer resonances of other states. This is explained schematically in figure 1.1 and 1.2. In the figure 1.2, the transition energy of $23p_{3/2} \rightarrow 24s_{1/2}$ of Cesium atoms has the same as the transition energy of $23p_{3/2} \rightarrow 23s_{1/2}$ in electric field $\approx$ 80 V/cm. Accordingly, if two Rubidium atoms (atoms A and B in figure 1.2) in state $23p_{3/2}$ with small separation, the collision and the productions of $23s_{1/2}$ and $24s_{1/2}$ (denoted by s and s') can occur following the energy transfers from $23p_{3/2} \rightarrow 24s_{1/2}$ transition to $23p_{3/2} \rightarrow 23s_{1/2}$ transition and afterwards both atoms eventually transfer these states to adjacent atoms (atoms C and D) at an appropriate separation.

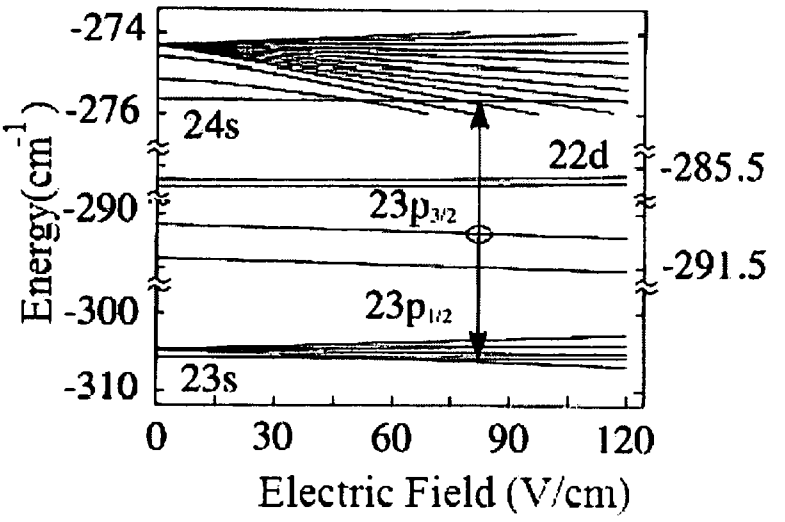

Figure 1.1: Energy levels of Cs in electric field, which there are some ranges of electric field strength that the energy transition of $23p_{3/2} \rightarrow 24s_{1/2}$ equals to the energy transition of $23s_{1/2} \rightarrow 23p_{3/2}$, and can lead to excitation exchange between two atoms initially in the $23p_{3/2}$ state[1].

After the study of this resonant dipole-dipole energy transfer, there was further study on effects of orientation of individual dipoles and spatial structure on the interaction transfer by Carroll et al.[3]. This lead to the study of one dimension energy transfer and possibility to transfer quantum information linearly through this energy transfer[4].

Rydberg atoms in electric fields is a possible candidate to form fast quantum phase gate according to their strong dipole interaction. There was first proposed by Jaksch[5]. The dipole-dipole interaction between two trapped neutral Rydberg atoms in a constant electric field can perform a quantum gate operation without entanglement with the motional states. The dipole-dipole interaction[6] between two atoms with the separation vector $\vec{R}$ is the first-order interaction and can be given as

$$V_{dd} = \frac{\vec{d_1}.\vec{d_2} - 3(\vec{d_1}.\hat{R})(\vec{d_2}.\hat{R})}{R^3}, \tag{1.1}$$

where $\vec{d_1}$ and $\vec{d_2}$ are electric dipole matrix elements. There are three states of atoms involved in the gate process. The first two states $|e\rangle$ and $|g\rangle$ of each

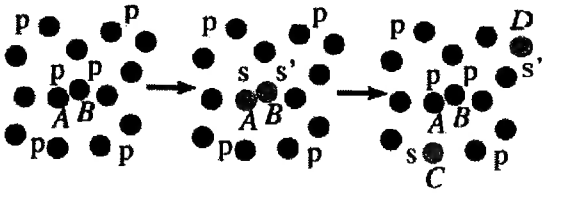

Figure 1.2: A schematic of excitation transfer in process corresponding to energy level in figure 1.1. Two Cs atoms (A and B)at $23p_{3/2}$ collide to produce $23s_{1/2}$ and $24s_{1/2}$ states and eventually transfer these s and s' states to the adjacent atoms(C and D).

atom following energy level scheme in figure 1.3 are served as the storage states of coherence time. The gate operation of the storage states is applied through exciting them to more loosely bound state $|r\rangle$ where the gate operation occurs by interaction with another atom. The phase gate transformation of two states $|e\rangle$ and $|g\rangle$ in figure 1.3 is defined[7] by

$$|a\rangle|b\rangle \rightarrow e^{i\varphi\delta_{a,g}\delta_{a,g}}|a\rangle|b\rangle, \tag{1.2}$$

where $|a\rangle$ and $|b\rangle$ are $|e\rangle$ or $|g\rangle$, $\delta_{a,g}, \delta_{a,g}$ are Kronecker symbols and φ is the phase shift of the entangle state. The phase shift is introduced into the two-atom operation by exciting the atoms in state $|g\rangle$ to Rydberg state $|r\rangle$ and drive back to $|g\rangle$ with subsequently phase shift φ, which can be controlled in the function of energy shift δ from the Rydberg state as a result of dipole-dipole interaction between atoms[5],[8]. However, the problem of implementation of a phase gate proposed by [5] is difficulty to control single atoms. More recently, Lukin et al.[9] proposed a quantum logic gate performed by collective excitation in a mesoscopic atomic ensembles using the idea of dipole blockade. Dipole blockade is the suppression of the excitation of a second atom arising from sufficient number and density of excited atoms. It is the result of energy perturbation of Rydberg atoms by adjacent atoms which shifts the energy level outside the wavelength of the coupling laser. Since the dipole-dipole interaction depends on the orientation of the dipoles, in order to increase the competence of the dipole blockade, the second-order interaction $-C_6/R^6$ called van der Waals interaction is exploited instead[10]. C_6 is a coefficient proportional to n^{11} for two np atoms[11].

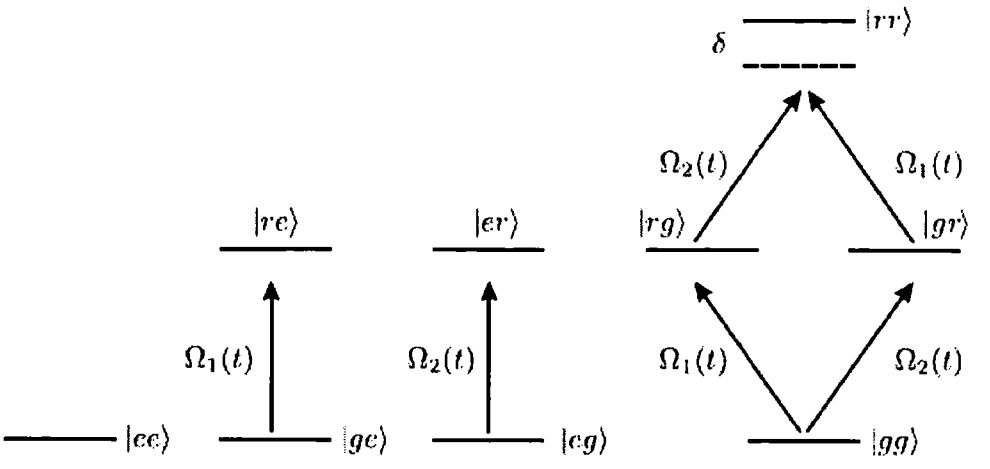

Figure 1.3: Schematic explanation of performing phase gate on single atoms with dipole-dipole interaction δ of two neutral atoms[5].

However, before further study on the interaction between Rubidium Rydberg atoms for quantum information can be completed, their behaviour in electric field has to be investigated in order to select which Rydberg state. Considering selection rule of atomic transitions, $|r\rangle$ state in the experiment is ns or nd following using $5S_{1/2}(F = 2)$ and $5P_{3/2}(F = 3)$ as $|e\rangle$ and $|g\rangle$, respectively. The principal quantum number n is considered by available laser systems. The calculation in this study will concentrate on d-states only. Moreover, this energy level profile is supposed to improve Rydberg atoms detection. The current study in Rydberg atoms by electromagnetically induced transparency(EIT) is used to study relation between experimental results and theoretical prediction[35]. Rydberg EIT is interesting as it offers a non destructive probe of Rydberg states.

In this project the energy levels in electric field of Rubidium atoms are investigated by the diagonalization-Hamiltonian method. Section 1.2 is basic description of Rydberg atoms. After this Rydberg atoms introduction the detail of diagonalization-Hamiltonian method and involving calculation will be explained in Chapter 2. The calculation methods using in Chapter 2 are subsequently tested by earlier studies both experimental and theoretical in Chapter 3. In this chapter we also present simplified Stark shift scaling laws.

Finally, the calculated Stark shifts are compared study with experimental spectra by EIT in Chapter 4.

1.2 Rydberg atoms

Historically, Rydberg atoms appeared in Physics for the first time in 1885, when Balmer found the formula,

$$\nu = \left(\frac{1}{4b}\right)\left(\frac{1}{4} - \frac{1}{n^2}\right), \tag{1.3}$$

where ν is wave number of the observed spectrum lines from a higher energy level to n=2, and the constant b=3645.6 $\AA$. Until 1890 Rydberg tried to classify other spectra of alkali atoms into three series, sharp(s), principal(p) and diffuse(d) using the equation

$$\nu_s = \nu_{\infty s} - \frac{Ry}{(n-\delta_s)^2}, \nu_p = \nu_{\infty p} - \frac{Ry}{(n-\delta_p)^2}, \nu_d = \nu_{\infty d} - \frac{Ry}{(n-\delta_d)^2}, \tag{1.4}$$

where $\nu_{\infty s}$, $\nu_{\infty p}$, $\nu_{\infty d}$ are the limit of series s, p, and d, respectively , δ_s, δ_p, and δ_d are quantum defect, and Ry, the Rydberg constant. The value of Rydberg constant discovered by Rydberg is 109721.6 cm^{-1}.

In 1913 Bohr proposed a model where obtains energy levels field and orbital radius in the terms of principal quantum number n,

$$E = -\frac{8\pi^2\varepsilon_0^2 Z^2 e^4 m}{\hbar^2}\left(\frac{1}{n^2}\right), \tag{1.5}$$

and

$$r = \left(\frac{\hbar^2}{4Ze^2 m\pi\varepsilon_0}\right)n^2, \tag{1.6}$$

respectively. As a result of (1.5) the Rydberg constant could be related to Bohr model by the formula,

$$Ry = \frac{8\pi^2\varepsilon_0^2 Z^2 e^4 m}{\hbar^2}. \tag{1.7}$$

Accordingly, Bohr's model implied two distinctive properties of Rydberg atoms. Firstly, according to dependence on n^2 in equation(2.1), it implied large orbit of valence electron at large n. Secondly, considering loosely binding energy of electron at high n in Coulomb field which depends on n^{-2}. Furthermore, other properties of Rydberg atoms are also able to be described by

Table 1.1: Properties of Rydberg atoms.

Property	n dependence
Binding Energy	n^{-2}
Orbital radius	n^2
Geometric cross section(πr^2)	n^4
Energy between adjacent states	n^{-3}
Dipole moment	n^2
Polarizability	n^7
Radiative lifetime	n^3
Fine-structure interval	n^{-3}
Dipole-dipole interaction	n^4
van der Waals interaction	n^{11}

dependence on the principal quantum number as showed in table 1.1. Using equation(1.5), we obtain the energy separation between adjacent states or fine structure interval

$$E_{n+\Delta n} - E_n = Ry\left[\frac{1}{n^2} - \frac{1}{(n+\Delta n)^2}\right] \simeq \frac{2Ry\Delta n}{n^3}. \tag{1.8}$$

The dipole moment which is defined by expectation value of er is determined by $n^{2\sigma}$ dependence property of expectation value of r^σ for $\sigma > 1$ analytically calculated by Bethe and Salpeter[14]. Since the polarizability α of state m depends on dipole moment and energy separation following the equation

$$\alpha = 2\sum_{i\neq m} \frac{|\langle m|r\cos\theta|i\rangle|^2}{E_m - E_i}, \tag{1.9}$$

we can evaluate the polarizability α in proportional to n^7 which explains the high sensitivity of Rydberg atoms to the electric fields. This exaggerate property of Rydberg atoms makes their energy levels easy to be controlled by electric fields, for instance, the energy levels requires for energy transfer previously introduced in figure 1.1 and 1.2 are controlled by a modest electric field of only $\sim 80V/cm$.

Chapter 2

Theory

Generally, the term Stark shift refers to a shift or splitting of an energy level as a function of an applied electric field. In this study we employ diagonalization of a Hamiltonian matrix for Rubidium atoms in external electric field to calculate Stark shifts including fine structure. This calculation in detail need calculation of energy levels without electric field by quantum defect theory and radial integral, which calculated by the Coulomb approximation method in this work.

2.1 The Hydrogen Atom

In order to study theoretical predictions for Rydberg atoms, we need to study the wave function, and the Hydrogen wave function is the simplest one to start with a provides a good model of many of the properties of Rydberg atoms.

Starting with Schrodinger equation of Hydrogen atom in atomic unit, which is

$$-\left(\frac{\nabla^2}{2}-\frac{1}{r}\right)\psi = E\psi, \tag{2.1}$$

where E is energy of electron ,∇^2 is defined in Spherical coordinate as

$$\nabla^2 = \frac{\partial}{\partial r^2}+\frac{2}{r}\frac{\partial}{\partial r}+\frac{1}{r^2\sin\theta}\frac{\partial}{\partial\theta}\left(\sin\theta\frac{\partial}{\partial\theta}\right)+\frac{1}{r^2\sin\theta}\frac{\partial^2}{\partial\phi^2}. \tag{2.2}$$

Table 2.1: Atomic units

Quantity	Atomic unit	Value
Mass	Electron Mass m_e	9.1×10^{-28} g
Charge	Electron charge e	1.6×10^{-19} C
Length	Radius of, the first Bohr orbit a_0	0.529 $\mathring{A}$
Energy	Twice the ionization potential of hydrogen E_h	27.2 eV
Velocity	Velocity of the first Bohr orbit $a_0 E_h/\hbar$	2.19×10^8 cm/s
Electric field	Field at the first Bohr orbit E_h/ea_0	5.14×10^9 V/cm

Atomic units are defined in table 2.1.

Assume that ψ can be separated into a product of two functions, i.e.

$$\psi = Y(\theta, \phi)R(r) \tag{2.3}$$

Consequently, the Schrodinger equation of Hydrogen atoms becomes two separate equations which are

$$\frac{r^2}{R}\left[\frac{\partial^2 R}{\partial r^2} + \frac{2}{r}\frac{\partial R}{\partial r} + 2\left(W + \frac{1}{r}\right)R\right] = -\frac{1}{Y}\left[\frac{1}{r^2 \sin\theta}\frac{\partial}{\partial\theta}\left(\sin\theta\frac{\partial Y}{\partial\theta}\right) + \frac{1}{r^2 \sin\theta}\frac{\partial^2 Y}{\partial\phi^2}\right] = \lambda, \tag{2.4}$$

where λ is positive integer. If $\lambda = l(l+1)$ the solution of the angular function is

$$Y_{lm}(\theta, \phi) = \sqrt{\frac{(l-m)!}{(l+m)!}\frac{2l+1}{4\pi}} P_l^m(\cos\theta)e^{im\phi}, \tag{2.5}$$

where $P_l^m(x)$ is associated Legendre polynomials, l is zero or a positive integer, and m is any integer from $-l$ to l.

The radial equation with $\lambda = l(l+1)$ can be expressed as

$$\frac{\partial^2 R}{\partial r^2} + \frac{2}{r}\frac{\partial R}{\partial r} + \left[2E + \frac{2}{r} - \frac{l(l+1)}{r^2}\right]R = 0. \tag{2.6}$$

By using simplified radial wave function $R(r) = \rho(r)/r$ substituted into (2.6)

$$\frac{\partial^2 \rho}{\partial r^2} + \left[2E + \frac{2}{r} - \frac{l(l+1)}{r^2}\right]\rho = 0. \tag{2.7}$$

If we analyze equation (2.7) asymptotically, it reduces to

$$\left[\frac{\partial^2 \rho}{\partial r^2} + 2E\right]\rho = 0, \tag{2.8}$$

which has the solution

$$\rho = e^{-r\sqrt{-2E}}. \tag{2.9}$$

This asymptotic behavior implies the form

$$\rho = f(r)e^{-r\sqrt{-2E}}. \tag{2.10}$$

Using a power series to solve 2.7 by substituting (2.10) by $f(r) = r^{l+1}g(r)$ and $g(r) = \sum_{k=0}^{\infty} c_k r^k$,when $c_0 \neq 0$. The final solution of $g(r)$ is the polynomial called associated Laguerre polynomial. That is

$$g_{n+l}^{2l+1}(r) = L_{n+l}^{2l+1}(r) = \sum_{k=0}^{n-l-1} (-1)^{k+1} \frac{[(n+l)!]^2 r^k}{(n-l-1-k)!(2l+1+k)!k!}, \tag{2.11}$$

where n is related to E by (1.5), which $Ry \approx 0.5$ au. Finally, the radial wave function can be written as

$$R_{nl}(r) = N_{nl} e^{-r/n} r^l L_{n+l}^{2l+1}(r), \tag{2.12}$$

where

$$N_{nl} = \left[\left(\frac{2}{n}\right)^3 \frac{(n-l-1)!}{2n[(n+l)!]^3} \right]^{1/2}, \tag{2.13}$$

is the normalized constant of wave function of the hydrogen. Seeing that asymptotic property of valence electrons of alkali Rydberg atoms and the total Coulomb charge is approximated to be unity and considered as a point charge comparing to large electronic radius, their asymptotic wave functions have the same form as Hydrogen wave function. Under these circumstances, the Hamiltonian equations of alkali Rydberg atoms differ from an equation describing Hydrogen at potential term using $V(r)$ which converges to $-1/r$ asymptotically. However, this implies the possibility to calculate the asymptotic wave function of other alkali Rydberg atoms by developing the Hydrogen wave function. Some experimental results were employed since $V(r)$ cannot be calculated analytically. They subsequently provided and introduced the crucial constants for Rydberg atomic study called quantum defect[32][12].

2.2 Quantum defect

The quantum defect (δ) was described in early spectroscopic experiments as small difference between the spectrum of alkali atoms and hydrogen. It

appears as the distortion in principal quantum number n of hydrogen as it can be described by energy level of hydrogenic atoms in the equation

$$E_n = \frac{-1}{2(n-\delta)^2} = \frac{-1}{2n^{*2}}. \tag{2.14}$$

It is showed by later experimental results that quantum defect depends on n, l, and j. In theoretical treatment of the quantum defect it is described as perturbation of core electron distribution and the nucleus on energy levels. Considering the large distance between the valence electron and the nucleus together with the core electrons of alkali Rydberg atoms, the behaviour of alkali valence electrons is very similar to the behaviour of the electrons of hydrogen. It follows that the radial Schrodinger equation of alkali atoms can be written as

$$\frac{\partial^2 \rho}{\partial r^2} + \left[2E + V(r) - \frac{l(l+1)}{r^2}\right]\rho = 0, \tag{2.15}$$

where $V(r)$ is the potential of nuclear charge and the spherically average charge distribution of the core electrons [15], which asymptotically converges to $-1/r$. Using the potential of Rubidium calculated by Klapisch[18], the asymptotically convergence of $V(r)$ is showed by figure 2.1.

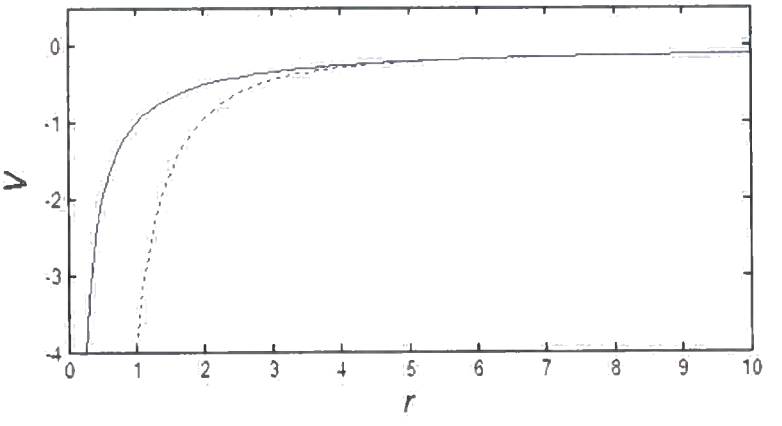

Figure 2.1: Comparison between Coulomb potential of Hydrogen(solid line) and the effective potential for one valence electron of Rubidium(broken line) introduced by Klapisch[18] in atomic unit.

Using Hartree's solution[16], Burgess and Seaton [17] calculated the radial

wave function with the quantum defect for large r as

$$R(r) = (2\pi E)^{-1/2}\cos(\delta)\sin(\zeta) + (2\pi E)^{-1/2}\sin(\delta)\cos(\zeta), \quad (2.16)$$

$$= (2\pi E)^{-1/2}\sin(\delta+\zeta), \quad (2.17)$$

where

$$\zeta = (2E)^{1/2}r - \frac{l\pi}{2} + \frac{1}{k}\ln(E/2)^{1/2}r + \arg\Gamma(l+1-i/k). \quad (2.18)$$

and $R(r) = \rho(r)/r$. The solution in equation (2.17) shows one obvious influence of the quantum defect on the wave function namely as the phase shift.

2.3 Stark Hamiltonian

The Hamiltonian used to describe single active electron for atoms in a static electric field is simply a sum of the electric field interaction potentials. It is written in atomic units as

$$V_F = Fz, \quad (2.19)$$

where F is the electric field lying along the z axis with the electric field independent Hamiltonian of the atom H_0. The term z is known as the dipole operator. Therefore, the total Hamiltonian can be expressed in atomic unit as

$$H = H_0 + V_F = -\frac{\nabla^2}{2} - \frac{Z}{r} + Fz, \quad (2.20)$$

when Z is an asymptotic charge in the Coulomb term of the Hamiltonian equation. As a result of considering core electrons and nucleus of alkali Rydberg atoms as an ionic core, the value of Z of alkali Rydberg atoms is one.

Although parabolic coordinate treatment to describe Hydrogen Rydberg atoms is sufficient to describe behaviour of Stark shift and appearance shape of atoms, it cannot be used to calculate the explicit Stark shift in alkali Rydberg atoms. One of those reasons is the significant size of the alkali ionic core and its inexplicit form of $V(r)$ for which the wave function is not analytically separable into parabolic coordinates [12]. Therefore the Spherical presentation of wave function is used in the calculation of Rubidium Rydberg

states in an electric field. However the patterns of the shifts in high l states are still able to be equivalently described by parabolic coordinate. Moreover, calculations using diagonalization where the energy eigenvalue of each state is calculated by direct diagonalizing the Hamiltonian matrix formed by coupling all spherical basis states to the Hamiltonian equation [26] is appropriate. To calculate Stark shifts but in low electric field strength calculation using the perturbation theory can be possibly used[31], because of its converge expansion in low electric field.

Generally, diagonalization method uses all of energy states to form the Hamiltonian matrix, which is defined by

$$H' = \begin{pmatrix} \langle 1|H|1\rangle & \langle 1|H|2\rangle & \cdots & \langle 1|H|N\rangle \\ \langle 2|H|1\rangle & \langle 2|H|2\rangle & \cdots & \langle 2|H|N\rangle \\ \vdots & \vdots & \ddots & \vdots \\ \langle N|H|1\rangle & \langle N|H|2\rangle & \cdots & \langle N|H|N\rangle \end{pmatrix}, \tag{2.21}$$

where N is number of all states. However, some states have negligible impact and need not to be included in the Hamiltonian matrix. According to Hamiltonian equation of this system, the calculated Hamiltonian matrix can be separated into two terms which are diagonal and off-diagonal. The diagonal term is obviously calculated by the H_0 term and the off-diagonal term is calculated by the V_F term of the Hamiltonian equation. We can regard the off-diagonal term as the field dependence term of the Hamiltonian matrix.The diagonal elements of the Hamilton matrix is calculated in the basis of $|njm_j\rangle$ where j is total angular momentum quantum number and m_j is secondary total angular momentum quantum number. They are calculated by the Rydberg formula[12]

$$\langle n, j, m_j|H_0|n, j, m_j\rangle = \frac{-R_{Rb}}{(n-\delta_{nlj})^2} = \frac{-R_{Rb}}{n^{*2}}, \tag{2.22}$$

where $R_{Rb} = 109\ 735.605\ \mathrm{cm}^{-1}$ is Rydberg constant for Rubidium atoms, n^* is quantum number with quantum defect δ_{nlj} which depends on n, l, and j. The quantum defect is calculated by the equation

$$\delta_{nlj} = \delta_0 + \delta_2/(n-\delta_0)^2. \tag{2.23}$$

δ_0 and δ_2 are the constants from the recent experiments on quantum defect

using cold rubidium atoms with $n > 20$, and $l < 3$, and experiment results in [12] for $l = 3$.The values of δ_0 and δ_2 are shown in table 2.2.

Table 2.2: Rb quantum defect constant(numbers between bracket are uncertainties of last digits)

Series	δ_0	δ_2
$ns_{1/2}$[32]	3.131 180 4(10)	0.178 4
$np_{1/2}$[32]	2.654 884 9(10)	0.2900(6)
$np_{3/2}$[32]	2.641 673 7(10)	0.2950(7)
$nd_{3/2}$[32]	1.348 091 71(40)	-0.602 86(26)
$nd_{5/2}$[32]	1.346 465 72(30)	-0.586 00(18)
$nf_{5/2}, nf_{7/2}$[12]	0.016312	0.064007

In the case that the series of l is higher than three, quantum defects are approximated to be zero. The dipole matrix elements are obtained by

$$\langle njm_j|z|n'j'm_j'\rangle = \langle nl|r|n'l'\rangle \sum_{m_l,m_l',m_s,m_s'} \langle l, s = 1/2, m_l, m_s|j, m_j\rangle \times \langle l', s' = 1/2, m_l', m_s'|j', m_j'\rangle \langle l, m_l|\cos\theta|l', m_l'\rangle, \quad (2.24)$$

[26] where the first and second terms in summation are Clebsch-Gordan coefficients transforming the $|n, j, m_j\rangle$ basis to the $|n, l, m_j, s, m_s\rangle$ basis in order to couple the states with $\cos\theta$ which depends on l and m_l, and r which depends on n and l .The last term in the summation is elementary algebra of spherical harmonics, which can be expressed in the term of Clebsch-Gordan coefficients,

$$\langle l, m_l|\cos\theta|l', m_l'\rangle = \sqrt{\frac{(2l'+1)}{(2l+1)}}\langle l', 0, 1, 0|l, 0\rangle\langle l', -m_l', 1, 0|l, m_l\rangle. \quad (2.25)$$

This equation implies the selection rule $m_l = m_l'$ and $l' = l \pm 1$. In addition, (2.24) can be further derived in the form of products of three Clebsch-Gordan coefficients, which implies the selection rules of $m_j' = m_j$ and $j' = j \pm 1$ [33]. In addition, the radial matrix elements $\langle nl|r|n'l'\rangle$ are calculated with the Coulomb approximation which is introduced in section 2.3. In figure 2.2,

which is representing the dipole matrix elements of Rb with $n = 20$, we can see the result of the selection rule by looking at non zero terms of the matrix elements, and also when the states in different principal quantum number n are used to form the matrix in figure 2.3. The strength of dipole

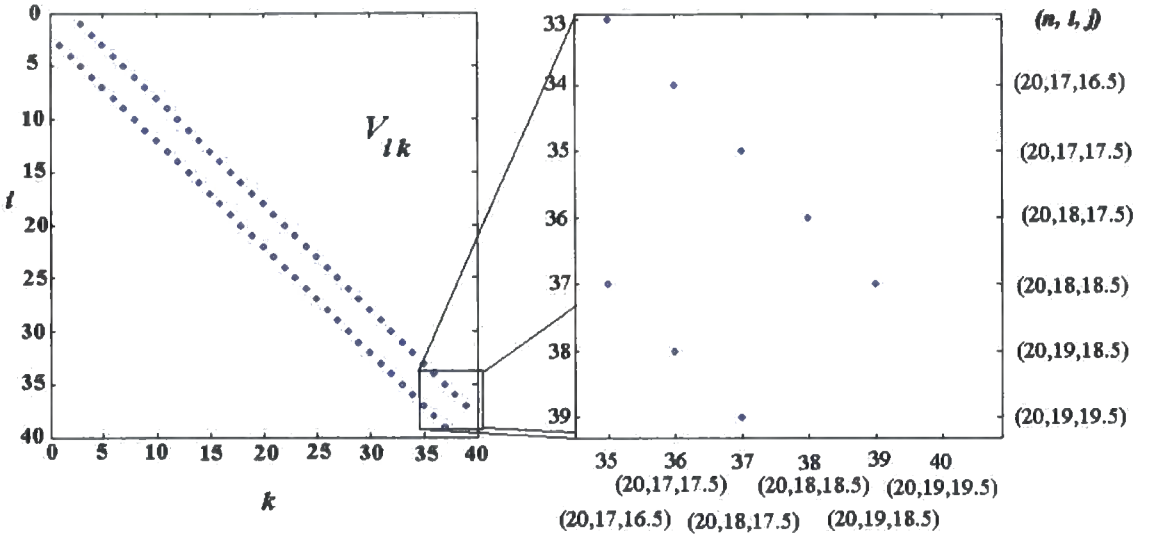

Figure 2.2: The non-zero elements (represented by dots) of dipole matrix formed by (2.24) and energy states $|n, l, j\rangle$ where $n = 20$, that are $|n = 20, l = 0, j = 0.5\rangle$, $|20, 1, 0.5\rangle$, $|20, 1, 1.5\rangle$, ..., $|20, 19, 18.5\rangle$,and $|20, 19, 19.5\rangle$. The white area of the graph represents zero matrix elements, i and k are row and column of the matrix, respectively. Obviously, the non-zero elements are only the horizontal and vertical adjacent elements of the subdiagonal and the superdiagonal. These dots also lie in two diagonal lines following increasing l or l'.

matrix elements corresponding to figure 2.3 is showed in the figure 2.4. In each group of matrix elements defined as dipole matrix elements between the group with same principal quantum number n and another group with same principal quantum number n' can be divided into two subgroups following continuous dipole matrix elements in the term of l. For example the group of dipole matrix elements coupling the states with $n = 20$ and $n' = 21$, there is one subgroup of $l > 3$ states which the strength of matrix elements

change continuously in the term of l and the another subgroup with $l \leq 3$ states which discontinuous matrix elements in the term of l. Considering the continuous strength matrix elements subgroups, the continuous pattern can be described by hydrogen like behavior of their energy levels since there is no effect of quantum defect. This makes radial term of equation (2.24) can be described by function of n and l:

$$\langle n^* l - 1|r|n^* l\rangle = \frac{3n}{2}(n^2 - l^2)^{\frac{1}{2}}, \tag{2.26}$$

which is the same equation described radial matrix elements $\langle nl - 1|r|nl\rangle$ of hydrogen. However, this part of the matrix element influences on permanent dipole moment pattern of states $l > 3$ in an electric field.

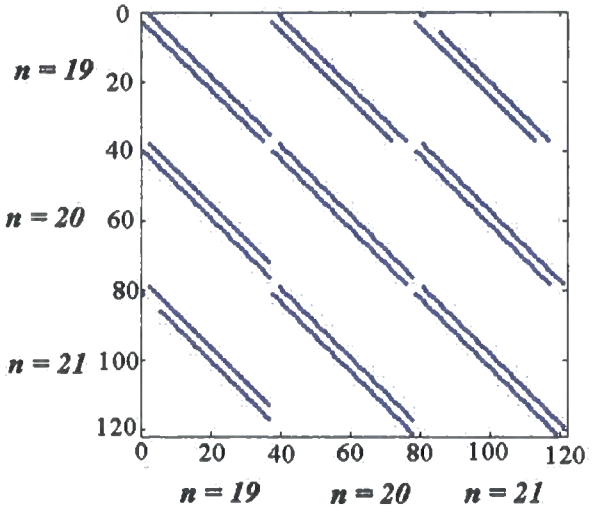

Figure 2.3: The non-zero elements (represented by dots) of dipole matrix formed by (2.24) and energy states $|n, l, j\rangle$ of three manifolds of $n = 19$, $n = 20$, and $n = 21$,i and k are row and column of the matrix, respectively. There are 9 block matrices denoted by the principal quantum number n of the horizontal basis states and n' of the vertical basis states are the clear resemblances to the dipole matrix in figure 2.2.

After we obtained the Hamiltonian matrix, each calculation is done by diag-

onalizing the Hamiltonian matrix at fixed F and m_j, which is written as

$$diagonalize\left[H^{'}\right] = diagonalize\begin{pmatrix} E_1 & FV_{12} & \cdots & FV_{1N} \\ FV_{21} & E_2 & \cdots & FV_{2N} \\ \vdots & \vdots & \ddots & \vdots \\ FV_{N1} & FV_{N2} & \cdots & E_N \end{pmatrix}$$
$$= \begin{pmatrix} E_1^{'}(F) & 0 & \cdots & 0 \\ 0 & E_2^{'}(F) & \cdots & 0 \\ \vdots & \vdots & \ddots & \vdots \\ 0 & 0 & \cdots & E_N^{'}(F) \end{pmatrix}, \quad (2.27)$$

where $V_{i,j}$ for $i,j = 1,2,3,...N$ is a product of angular and radial matrix elements (i,j). To form the line of Stark shift in the term of F, calculations are done by calculating $F + jdF$ in very small interval dF in figure 2.5.

2.4 Radial Integral

Generally, radial transition in Atomic Physics can be written into Dirac notation and equivalent integral form as

$$\langle nl|r^q|n'l'\rangle = \int_0^\infty dr r^2 R^*_{n,l}(r) R_{n',l'}(r) r^q. \quad (2.28)$$

According to the solution of Schrodinger equation (2.7) in Chapter 2, the radial transition for hydrogen is obtained explicitly by solution of equation (2.7) which W is substituted by $-1/2n^2$ and integrated in equation (2.28) by Gordon[20] in the series of a Gaussian hypergeometric function ${}_2F_1$ [19].

2.4.1 Coulomb approximation

Since there are similarity behaviours between hydrogen and hydrogenic Rydberg atoms, which in this study particularly focus on Rubidium Rydberg atoms, the calculation of radial integration has similar process. The value of W substituted in (2.7) uses energy level of Rydberg atom including quantum defect, which is

$$W = \frac{-1}{2(n-\delta_{nlj})^2} = \frac{-1}{2n^{*2}}, \quad (2.29)$$

where the constant two appears in equation (2.29) is the approximated Rydberg constant of any atoms in atomic unit.

Since the quantum defects are not integer, the effects of quantum defects on analytical solution of R_{nl} are forbid expression in Laguerre polynomial which is summation of integer of $n-l-1$. Whittaker[19] proposed the solution of the differential equation

$$\frac{\partial^2 R}{\partial r^2} + \frac{2}{r}\frac{\partial R}{\partial r} + \left[\frac{2}{r} - \frac{l(l+1)}{r^2} - \frac{1}{n^{*2}}\right] R = 0, \tag{2.30}$$

where n^* is not integer with boundary condition,

$$R_{n,l} \to 0 \qquad \text{as} \qquad r \to \infty, \tag{2.31}$$

which satisfies the property of Rydberg atoms. This condition was applied to evaluate equation (2.28) by Bates and Damgaard[21] is called in the term of Coulomb approximation. The solution of 2.30 is

$$R_{n,l} = \frac{(2r/n^*)^{n^*} e^{-r/n^*}}{n^{*2}\Gamma(n^*+l-1)\Gamma(n^*-l)} \left(1 + \sum_{t=1}^{\infty} \frac{a_t}{r^t}\right), \tag{2.32}$$

where

$$a_1 = \frac{n^*}{2}\left[l(l+1) - n^*(n^*-1)\right], \tag{2.33}$$

and

$$a_t = a_{t-1}\left\{\frac{n^*}{2t}\left[l(l+1) - (n^*-t)(n^*-t+1)\right]\right\}. \tag{2.34}$$

By rearranging equation (2.32), the equation (2.28) where $s = 1$ can be written in the gamma function form

$$\int_0^\infty dr R^*_{n,l}(r) R_{n',l'}(r) r = \sum_{t=0}^{\infty}\sum_{t'=0}^{\infty} \int_0^\infty dr c_t(n^*,l) c_{t'}(n^{*'},l') r^{(n^*+n^{*'}-t-t'+1)} e^{-r\left(\frac{n^{*'}+n^*}{n^{*'}n^*}\right)},$$

$$= \sum_{t=0}^{\infty}\sum_{t'=0}^{\infty} c_t(n^*,l) c_{t'}(n^{*'},l') \left(\frac{n^{*'}+n^*}{n^{*'}n^*}\right)^{(n^*+n^{*'}-t-t'+2)} \Gamma(n^*+n^{*'}-l-l'+1) \tag{2.35}$$

where

$$c_t = \frac{a_t}{2t}\left[l(l+1) - (n^*-t)(n^*-t+1)\right]. \tag{2.36}$$

Considering radial integral in the form of asymptotic expansion, the term with $n^* + n^{*'} - l - l' > 1$ can be ignored.

Finally, Bates and Damgaard proposed the result of

$$\langle n^*l-1|r|n^*l\rangle = \frac{3n^*}{2}(n^{*2}-l^2)^{\frac{1}{2}}, \tag{2.37}$$

and tables of calculated values in the term of $n^*-n^{*'}$ with intervals of 0.1 and n^* with intervals of 0.5 which leads to possibility to interpolate $\langle n^*l-1|r|n^{*'}l\rangle$ for closer interval of n^* and $n^{*'}$ in further study.

2.4.2 Numerical Modified Coulomb approximation

This section is developed method of Coulomb approximation of Bates and Damgaard in order to modify numerical method for any $n^*, n^{*'}, l$, and l' in equation (2.28) for q=1 by Edmonds et al.[28]. This work begin by using extrapolation considered by Picart et al. [27] which extrapolated the tables calculated by Bates and Dangaard introduced in section 2.4.1. They proposed the function

$$\phi(n^*,l,n^{*'},l') = \langle n^*,l|r|n^{*'},l'\rangle / \left\{\frac{3}{2}n_c^2\left[1-\left(\frac{l_c}{n_c}\right)^2\right]^{1/2}\right\}, \tag{2.38}$$

where

$$l_c = max(l,l') \tag{2.39}$$

and

$$\frac{1}{n_c} = \frac{1}{2}\left[\left(\frac{1}{n^*}+\frac{1}{n^{*'}}\right)\right]. \tag{2.40}$$

The denominator in (2.38) is in the same form of $\langle n_c,l|r|n_c,l'\rangle$ calculated by Bates and Damgaard's Coulomb approximation. Therefore, the function (2.38) can be considered as a ratio of $\langle n^*,l|r|n^{*'},l'\rangle$ and $\langle n_c,l|r|n_c,l'\rangle$, which obviously converges to unity if $n^* \approx n^{*'}$. Using Maclaurin series expansion for ϕ in the term of $\gamma = l_c(l'-l)/n_c$ and application of Naccache's study[29] which calculated $\langle n,l|r|n',l'\rangle$, for n and n' are integer, sufficient small $s \equiv (n^*-n^{*'})$, Picart et al. obtained

$$\begin{aligned}\phi(n,l,n',l') &= \phi|_{\gamma=0} + \gamma\frac{\partial\phi}{\partial\gamma}\Big|_{\gamma=0} + \frac{\gamma^2}{2!}\frac{\partial^2\phi}{\partial\gamma^2}\Big|_{\gamma=0} + \ldots \\ &= \sum_{p=0}^{\infty}\gamma^p f_p(s),\end{aligned} \tag{2.41}$$

where $f_p(s)$ can be written in Bessel function:

$$\begin{aligned} f_0(s) &= f_2(s) = \frac{(-1)^s}{3s}(J_{s+1}(s) - J_{s-1}(s)) \\ f_1(s) &= \frac{(-1)^s}{3s}(J_{s+1}(s) + J_{s-1}(s)) \\ f_3(s) &= \frac{s}{2}f_0(s) + f_1(s), \end{aligned} \tag{2.42}$$

In later study, Edmonds et. al.[28] used Edmonds-Kelly method to modify (2.38) in order to calculate $\langle n^*, l|r|n^{*'}, l'\rangle$ which available for s is non-integer and obtained equation

$$\begin{aligned} \phi(n^*, l, n^{*'}, l') &= \phi|_{\gamma=0} + \gamma\frac{\partial\phi}{\partial\gamma}\Big|_{\gamma=0} + \frac{\gamma^2}{2!}\frac{\partial^2\phi}{\partial\gamma^2}\Big|_{\gamma=0} + \ldots \\ &= \sum_{p=0}^{\infty}\gamma^p g_p(s), \end{aligned} \tag{2.43}$$

where the values of g_p for p =0, 1, 2, and 3 are showed in the table 4 of [28] and figure 2.7, which are available for s between -4.0 and 4.0. In the case that the value of s is intermediate values in the interval of 0.05, g_p is evaluated by four-point interpolation [30] recommended by Edmonds et al.[28]:

$$\begin{aligned} g(s_0 + ha) \approx &-\frac{a(a-1)(a-2)g(s_{-1})}{6} + \frac{(a^2-1)(a-2)g(s_0)}{2} \\ &-\frac{a(a+1)(a-2)g(s_1)}{2} + \frac{a(a^2-1)g(s_2)}{6}, \end{aligned} \tag{2.44}$$

where h is the interval of s and $s_{-1} = s_0 - h, s_1 = s_0 + h$, and, $s_2 = s_0 + 2h$, following figure 2.6 are values of s in the table 4 of [28], and $s_0 + ha$ is intermediate point between s_0 and s_1. The function $g_p(s)$ is taken to be zero for $p > 3$.

After $\phi(n^*, l, n^{*'}, l')$ is evaluated, we obtain

$$\langle n^*, l|r|n^{*'}, l'\rangle = \left\{\frac{3}{2}n_c^2\left[1 - \left(\frac{l_c}{n_c}\right)^2\right]^{1/2}\right\}\sum_{p=0}^{3}\gamma^p g_p(s), \tag{2.45}$$

where $-4.0 \leq s \leq 4.0$, following [28].

2.4.3 Alternative methods of Radial Integral Calculation

Generally, there are two treatments of calculate radial integral, one is Coulomb approximation which has already been introduced in earlier subsection of this chapter. In additions to improved coulomb approximation of Bates and Damgaard by Whittaker equation and Edmonds and Kelly's extrapolation, there are some other calculations with different rearrangements of Whittaker equation[23]. For example, calculation using contour integral representation of Whittaker equation by Hylleraas[24] and calculation employing orbital quantum defect substituted into Whittaker equation done by Klarsfeld[23]. However, since these methods initially used Coulomb approximation idea, they eventually provided the same calculation accuracy. Another calculation method entirely differs from Coulomb approximation. It is proposed by Davydkin and Zon[37] using WKB approximation and classically considering electron as moving particle beyond Kepler's law. The method is recommended by Davydkin and Zon themselves that can be used sufficiently in high principal quantum numbers. The results proposed by Davydkin and Zon can be written as

$$\begin{aligned}\langle n^*, l|r|n^{*'}, l\rangle = \frac{\bar{n}^*}{Z\triangle}\left\{\frac{\sin\pi\triangle}{\pi\triangle}\left[\triangle(1-\varepsilon) \mp \frac{\sqrt{1-\varepsilon^2}}{\varepsilon}\right]\right\} \\ + \frac{\bar{n}^*}{Z\triangle}\left\{\frac{d}{dx}J_\triangle(-x) \mp \frac{\sqrt{1-\varepsilon^2}}{\varepsilon}J_\triangle(-x)\right\},\end{aligned} \tag{2.46}$$

where

$$\bar{n}^* = \sqrt{n^* n^{*'}}, \tag{2.47}$$

$$\varepsilon = \sqrt{1 - \frac{\left(l \mp \frac{1}{2} + \frac{1}{2}\right)^2}{(\bar{n}^*)^2}}, \tag{2.48}$$

$$\triangle = n^{*'} - n^*, \tag{2.49}$$

$$x = \varepsilon\triangle, \tag{2.50}$$

$J_\triangle(x)$ is Anger function

$$J_\triangle(x) = \frac{1}{\pi}\int_0^\pi \cos(\triangle\theta - x\sin\theta)d\theta. \tag{2.51}$$

In accuracy test by Kishimoto[38], equation(2.46) is recommended to be used high sufficiently for radial integral with $n > 100$.

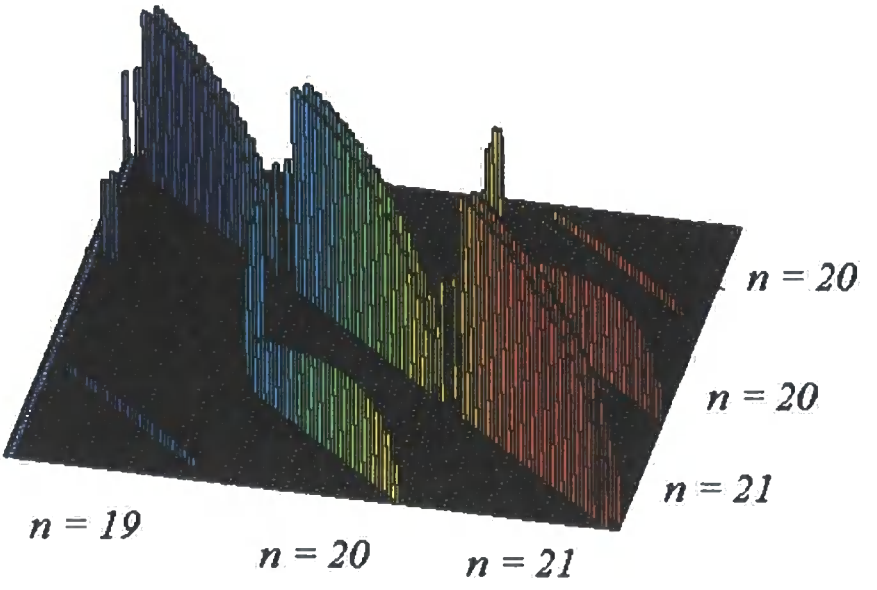

Figure 2.4: The bar graph shows strength of dipole matrix elements corresponding to the matrix in figure 2.3. Non-zero elements in each block matrices (n, n') resembling the dipole matrix in figure 2.2 can be divided into two subgroups by continuous of the strength of dipole matrix elements as a function of l which is clearly seen in the block matrices with $n = n'$ and $n = n' \mp 1$. The continuous subgroups are the set of coupling states with l and $l' > 3$.

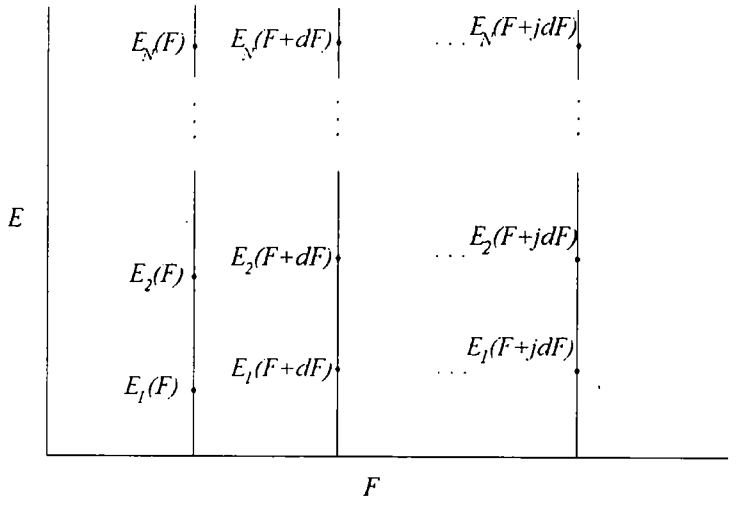

Figure 2.5: Calculation forming Stark shifts by diagonalization using N states as basis of Hamiltonian matrix. Calculation is done by diagonalizing the Hamiltonian matrix which depends on electric field F. Subsequently, we obtain a set of dots represent energy states N in constant electric field F, then do further calculation of constant electric field $F + jdF$ in small interval dF until dots form as the shift or splitting lines.

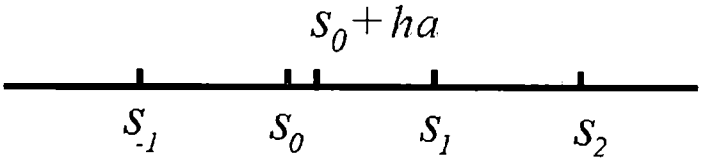

Figure 2.6: Four-point interpolation of the value of $g(s_0 + ha)$ by equation (2.44).

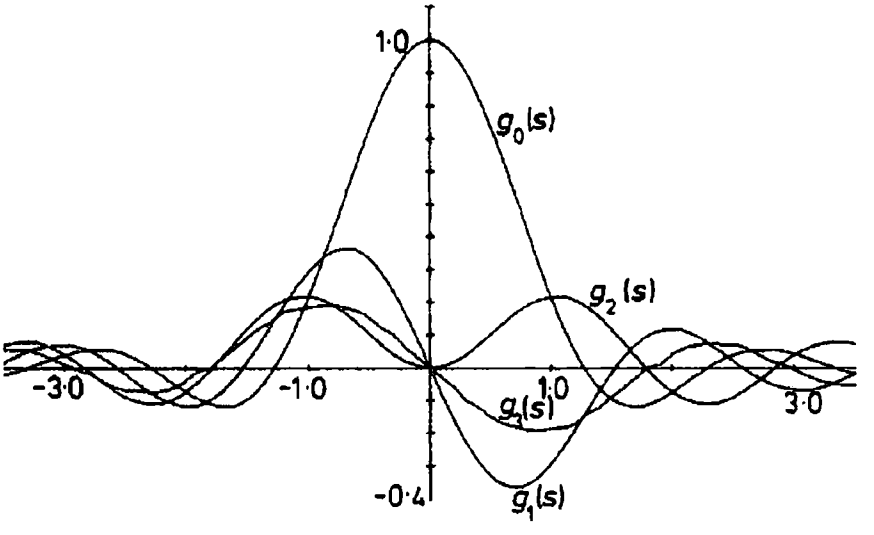

Figure 2.7: Graph of $g_0(s), g_1(s), g_2(s)$, and $g_3(s)$ extracted from table 4 of [27].

Chapter 3

Numerical tests

The first numerical test is the comparison results of non-relativistic Stark shifts between calculation using Coulomb approximation and exact calculation using Klapisch analytic potential [18]. Although Klapisch potential can provide high precision results in non-relativistic calculation, it is unable to be modified for fine splitting Stark shifts. Accordingly, these tests performed in order to understand precision of Coulomb approximation for non relativistic calculation which will be applied for fine splitting case. The second test is an examination whether the limitation of Coulomb approximation is adequate for Stark shifts calculation by testing the convergence of the states added to the calculated system. In the following section, Stark shifts with fine splitting calculations are tested in order to verify precision of Coulomb approximation comparing to another entirely different radial integral calculated by Davydkin and Zon[37]. After, since the diagonalization can be systematically anticipated some difficulties in higher n calculation, we lastly test possibility of using the scaling law to simplify Stark shifts with very high n and low field strength calculation.

3.1 Radial integral test

Due to the reason that each numerical calculation of radial integral is particularly sufficient in various regions of principal quantum number[22], the accuracy of applied radial integral method has to be checked in considered

states of Rydberg atoms. In this test the non-relativistic Stark shifts of two different calculations are compared. The first calculation is a diagonalization calculation using radial integral by Coulomb approximation in chapter 2. The non-relativistic dipole matrix element $\langle z \rangle$ reduces to n, l, and m_l dependence in equation (2.24), which is

$$\langle nlm_l|z|n'l'm_l'\rangle = \langle nl|r|n'l'\rangle \times \langle l, m_l|\cos\theta|l', m_l'\rangle. \tag{3.1}$$

Using equation (3.1), we obtain the non-relativistic Stark shift with $m_l = 0$ showed by figure 3.1. For $l > 3$ in the manifold, graphs show behaviour of hydrogen-like, by the result of negligible quantum defect.

Without evaluation of quantum defect directly, the energy level in equation (2.22) is calculated by Klapisch potential

$$V(r) = -\frac{1}{r}\left(1 + Ae^{-\alpha r} + Bre^{-\beta r}\right), \tag{3.2}$$

where $A = 36$ a.u., $B = 6.43527$ a.u., $\alpha = 3.33355$ a.u. and $\beta = 1.3698$ a.u.[18] as a screened Coulomb potential of Rubidium in the Hamiltonian:

$$H = -\frac{\nabla^2}{2} + V(r). \tag{3.3}$$

The results of the calculation are showed in figure 3.1. After obtaining the calculation results, the comparison calculation using program developed by Potvliege[25] is performed. The calculation in this program uses Sturmian wave function as radial wave function with high accuracy non-relativistic radial integral. Since using Klapisch potential as a screened Coulomb potential, this program is incapable to calculate systems with fine structure which have no analytical Hamiltonian function. Therefore, this comparison test is done in order to check the precision of the radial integral using Edmonds-Kelly method with is capable to be modified to calculate Stark shifts with fine structure. The comparison results are showed in figure (3.2). The graph shows agreement in low electric field strength and slightly difference in sufficient high strength field.

3.2 Convergence with number of states

Since Stark shifts calculated by diagonalization use all of the energy states as basis states of Hamiltonian matrix elements, the more states used for

calculation, the more accuracy calculation obtained. Nevertheless, diagonalization of very large matrix elements spends vast time to calculate. In order to calculate sufficiently and simply, the proper number and selection of basis states have to be considered. Fortunately, Edmonds-Kelly Coulomb approximation has limit condition for $|n'^* - n^*| < 4$ to terminate other unnecessary states to calculate the matrix elements. This termination is more reasonable when we look into the strength of dipole transition in the dipole matrix. In figure 2.4 considering the dipole transition between manifolds, the strength of dipole transition decreases as the difference of n. In figure 3.3, considering 20d states there are two sets of states in p state and f state which both set are the set of nearest energy states with 20d. The highest n of each set is the nearest one. This graph explains that the nearer energy the higher strength of dipole transition. The magnitude of dipole transition of the first p and f states in this graph are small enough to be negligible.

In addition, to understand the numerical influence of this termination on precision of Stark shifts, we do numerical test of the convergence of Stark shifts corresponding to the states added into the Hamiltonian matrix. The first test in figure 3.4 considering effect in the addition of the state 36p, 37p, 35p, and 38p, respectively, on the calculation of 35d state in an electric field. Using p-states as a convergence testing is selected on the basis of concentrating on Stark shifts of d-states in this project. The order of added states in this convergence testing follows the order of ascending different occupied energy between 35d state and each p-state, considering difference in quantum number dependence of the dipole transition. The blue line is the initial line which is the calculation using all states except p-states corresponding to the condition $|n'^* - n^*| < 4$. The red line is the calculation with addition of the 36p state in to the calculation of the blue line. After adding 37p, 35p, and 38p states, respectively, the shift converges to the black line. These results show the sufficient effect of two nearest added states, the upper and lower ones. Dealing with the effect of f-states on d-states in an electric field, the same test is done in similar way to the previous test with p-states. The f-states in this test are 34f, 33f, 35f, and 32f are added to Hamiltonian which consists of all states except f-states corresponding to the condition $|n'^* - n^*| < 4$, respectively. The results showed in figure 3.5, where the blue

line is the calculation without f-states in the Hamiltonian matrix. The red line is the calculation when the 34f state is added in the Hamiltonian matrix in the calculation of the blue line. Finally, after the 33f state was added into calculation, the result graph converges to black line, which is the same as when 35f and 32f are added respectively to calculation. These results are relevant to the results of p-states test that using two nearest states included the in Hamiltonian matrix is adequate to calculate precision Stark shifts of d-states.

3.3 Comparison with calculation using other radial integral method

Comparing this calculation to the earlier studies, the first comparison between figure 3.6 which is a calculation with fine splitting with $|m_j| = 1/2$ using Edmonds-Kelly method, and figure 3.7[31] is the calculation using Coulomb approximation of Zon and Davydkin[37]. This Coulomb approximation is described in section 2.4.3 as an alternative method to calculate radial integral. The results from both calculations are exactly the same in the order of the interval energy as shown in the graphs. They explain the identical behavior of calculation by diagonalization and the accuracy between both Coulomb approximation methods.

In order to compare the precision of the dipole matrix elements, we compare second-order coefficients of several np-states in table 3.1 which is defined by the summation in the first term of an equation describing Stark shift (δE) of state $|m\rangle$ in perturbation theory treatment[31] written as

$$\delta E = \sum_{i \neq m} \frac{\langle m|r\cos\theta|i\rangle\langle i|r\cos\theta|m\rangle}{E_m - E_i} F^2 + \sum_{i,k,p \neq m} \frac{\langle m|r\cos\theta|i\rangle\langle i|r\cos\theta|k\rangle}{E_m - E_i} \times \frac{\langle k|r\cos\theta|p\rangle\langle p|r\cos\theta|m\rangle}{(E_m - E_p)(E_m - E_k)} F^4, \quad (3.4)$$

where $|i\rangle, |k\rangle$ and $|p\rangle$ are states involving Stark shift calculation of state $|m\rangle$.

The precision of both theoretical results are close to each other and calculations using Edmonds-Kelly method are slightly better for n=46, 53 and

n	Order	$p_{1/2}, \|m_j\| = 1/2$			$p_{3/2}, \|m_j\| = 1/2$			$p_{3/2}, \|m_j\| = 3/2$		
		the.[a]	*the.*[b]	*exp.*[a]	*the.*[a]	*the.*[b]	*exp.*[a]	*the.*[a]	*the.*[b]	*exp.*[a]
46	10^{-3}	-2.721	-2.873	-2.77(6)	-3.190	-3.239	-3.30(7)	-2.723	-2.713	-2.77(6)
53	10^{-3}	-7.66	-8.107	-7.95(21)	-8.99	-9.133	-9.27(21)	-7.69	-7.67	-7.82(18)
59	10^{-2}	-1.672	-1770	-1.67(5)	-1.963	-1.993	-1.98(5)	-1.681	-1.676	-1.65(6)
70	10^{-2}	-5.76	-6.107	-5.98(21)	-6.77	-6.87	-7.10(22)	-5.81	-5.79	-5.90(19)
81	10^{-1}	-1.647	-1.747	-1.86(15)	1.936	-1.966	-2.18(11)	-1.663	-1.660	-1.87(11)

Table 3.1: Comparison between calculated and experimental results of second-order coefficient defined by equation(3.4) studied by Haseyama et al.(a)[31] and calculations by using Edmonds-Kelly method calculated radial matrix elements(b) of $p_{1/2}$ for $|m_j = 1/2|, p_{3/2}$ for $|m_j = 1/2|$ and $p_{3/2}$ for $|m_j = 3/2|$.The numbers between bracket of experimental results are uncertainties of last digits.

59.

3.4 Scaling laws

Although diagonalization is one of the sufficient methods to calculate Rubidium Rydberg atoms in an electric field as can be seen in some earlier tests, vast calculations, computing memory and time consumption are major problems of concerns since the number of matrix elements depend on number of included basis states in the power of 2. We have found that these vast calculations can be avoided when the calculations concentrating on low electric field regime are calculated by perturbation theory. The equation of perturbation theory treatment is expressed at equation (3.4) in the previous section. We consider only first term of equation (3.4) because low electric fields are considered for regime which F^2 is small enough for the second term to be neglected. The basis used in the calculation are only the states with following the selection rule $l' = l \pm 1$ of azimuthal quantum number l of the calculating states. In the example of the 41d state calculation, the number of the states dramatically decreases from 318 states or 101124 matrix elements to 17 states or 289 matrix elements or ~350 times faster. The example calculations of 50d states is showed in figure 3.8 which explains capability

of perturbation approach in the low-field regime. However, using table 1.1 and equation(3.4), the difference between adjacent Stark shifts (ΔE) can be written as a scaling function by n^* of F[31] as

$$\Delta E n^{*3} = F^2 \alpha n^{*10} + F^4 \beta n^{*20}, \tag{3.5}$$

where αn^{*10} and βn^{*20} are the differences between the second-order coefficients and fourth-order coefficients of two adjacent states defined by equation (3.4) written as functions of n^*. The power of 10, 20 and 3 of the equation are derived by n^{*2} dependence of dipole moments and n^{*3} dependence of two adjacent states and substitute into equation (3.4). Using (3.6), we are also able to defined low field regime by inequality

$$F^2 \ll \frac{\alpha}{\beta} n^{*-10}. \tag{3.6}$$

Finally, the shifts in the relationship between very low electric field and the energy difference between difference m_j shifts can be simplified by the scale transformation $F^{*2} = n^{*7} F^2$. The equation of this scaling can be written as

$$\Delta E = \alpha F^{*2}. \tag{3.7}$$

The scaled graph is showed in figure 3.9, where (i) for $\Delta E = |E(n, l = 2, j = 3/2, m_j = 1/2) - E(n, l = 2, j = 3/2, m_j = 3/2)|$ calculations ,(ii) for $\Delta E = |E(n, l = 2, j = 5/2, m_j = 1/2) - E(n, l = 2, j = 5/2, m_j = 3/2)|$ calculations and (iii) for $\Delta E = |E(n, l = 2, j = 5/2, m_j = 3/2) - E(n, l = 2, j = 5/2, m_j = 5/2)|$ calculations.

We obtain $\alpha_i \approx 3.06 \times 10^{-15} MHz.V^{-2}.cm^2$, $\alpha_{ii} \approx 1.28 \times 10^{-15} MHz.V^{-2}.cm^2$ and $\alpha_{iii} \approx 2.56 \times 10^{-15} MHz.V^{-2}.cm^2$ which are constant of scaling relations. These constants are less precise for lower Rydberg states and the shifts eventually converge to them following increasing n since s in equation (2.38) converges to zero. However, although the scaling law can show possible high efficiency results simplifying Stark shifts in high n, the exact field region and its accuracy evaluation are still crucial in practical uses. The figure 3.9 is a good example of this point owing to the distinguishable scattering of each state calculation with different n as a result of individual low field regimes or individual low α/β for each calculation following the definition by inequality (3.6).

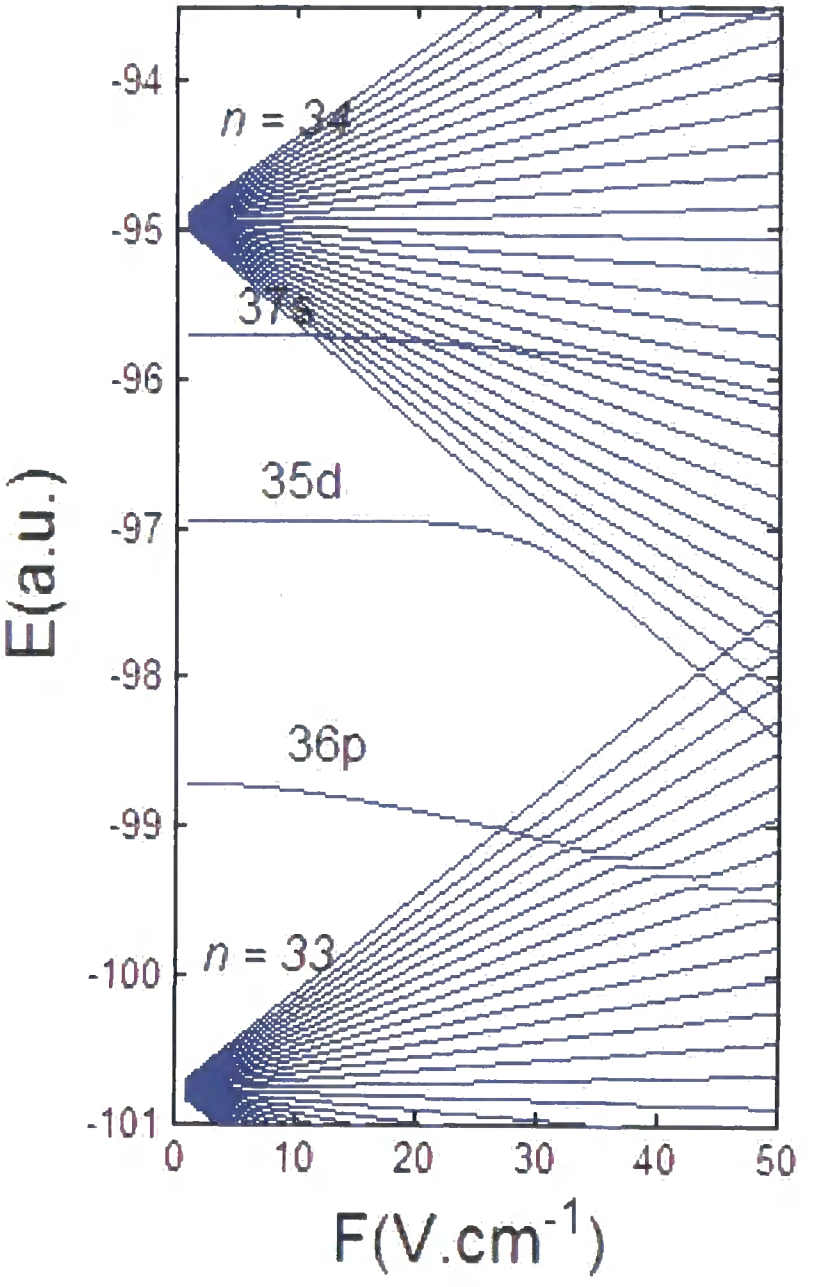

Figure 3.1: non-relativistic Stark shifts of Rubidium calculation by radial integral Edmonds-Kelly method.

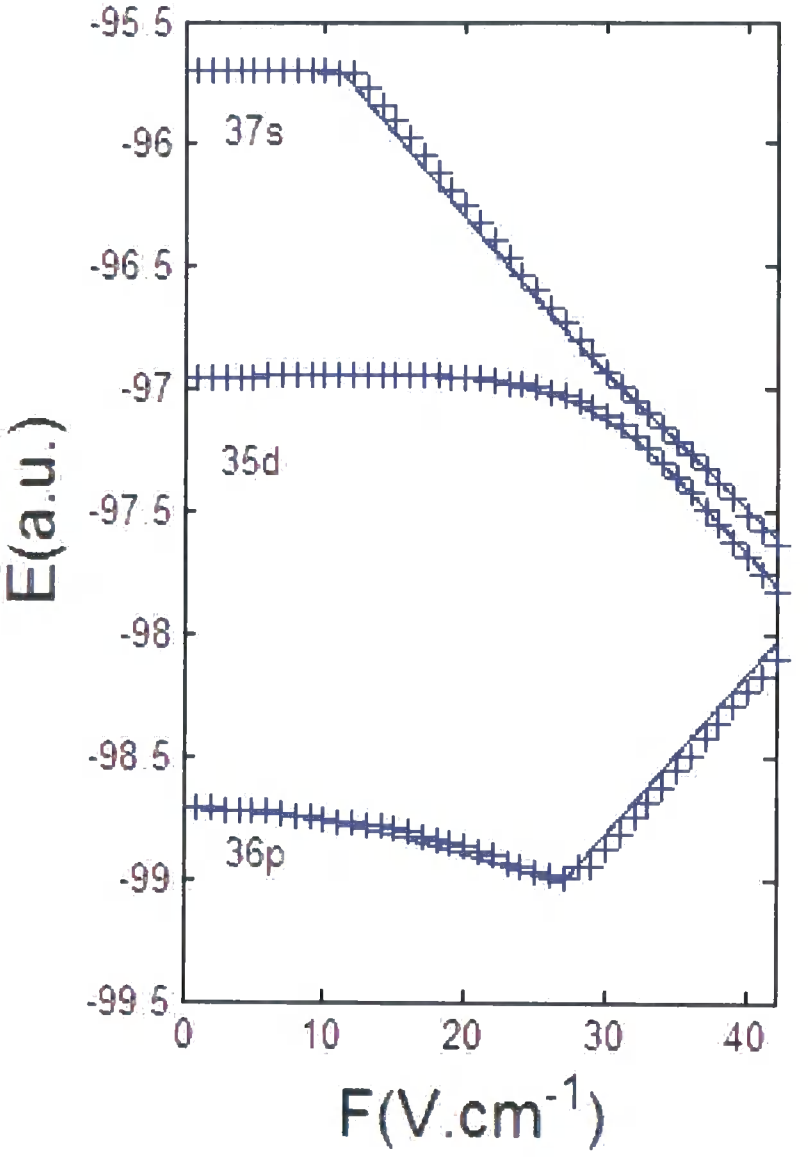

Figure 3.2: Comparison of non-relativistic Stark shifts of Rubidium at 35d, 37s and 36p between calculation by radial integral Edmonds-Kelly method(solid line) and the calculation by Sturmian wave function(+) in the region of electric field strength lower than field ionized regime with $m_l = 0$.

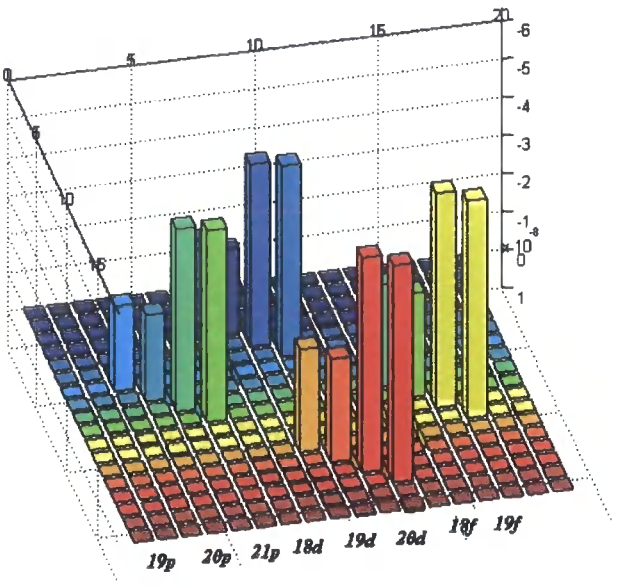

Figure 3.3: The bar graph shows the strength of dipole matrix elements formed by the nearest energy states p,f around 20d including 19d and 18d.

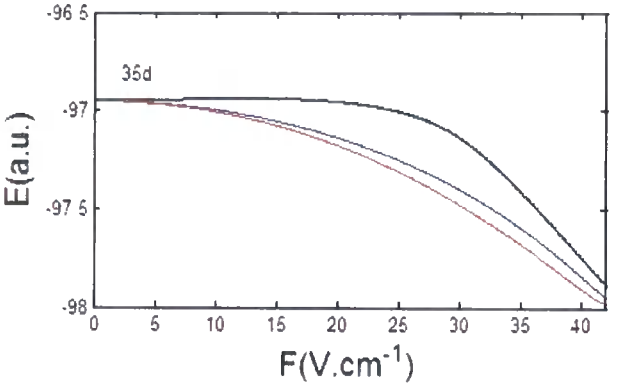

Figure 3.4: The graph illustrates convergence of Stark shifts of 35d as a result of addition 36p, 37p, 35p, and 38p states, respectively, into basis set of calculation. Where the blue line is calculated by using s-states, d-states, f-states and all states with $l > 3$, the red line is calculation including 36p state, and black line is calculation including 36p and 37p states. In addition, the results including other p-states are the black line.

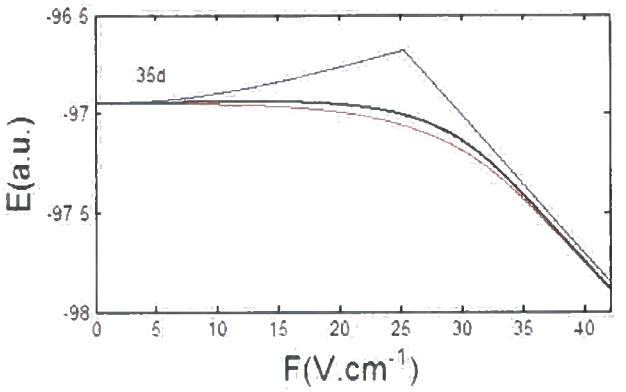

Figure 3.5: Convergence of Stark shift of 35d influenced by f-states. The calculation using all states with $l \neq 3$ is showed by the blue line. Calculation with addition of the nearest f-state(34f) into calculation of the blue line is showed by the red line, and the black line shows calculation by including other f-states into calculation of the red line.

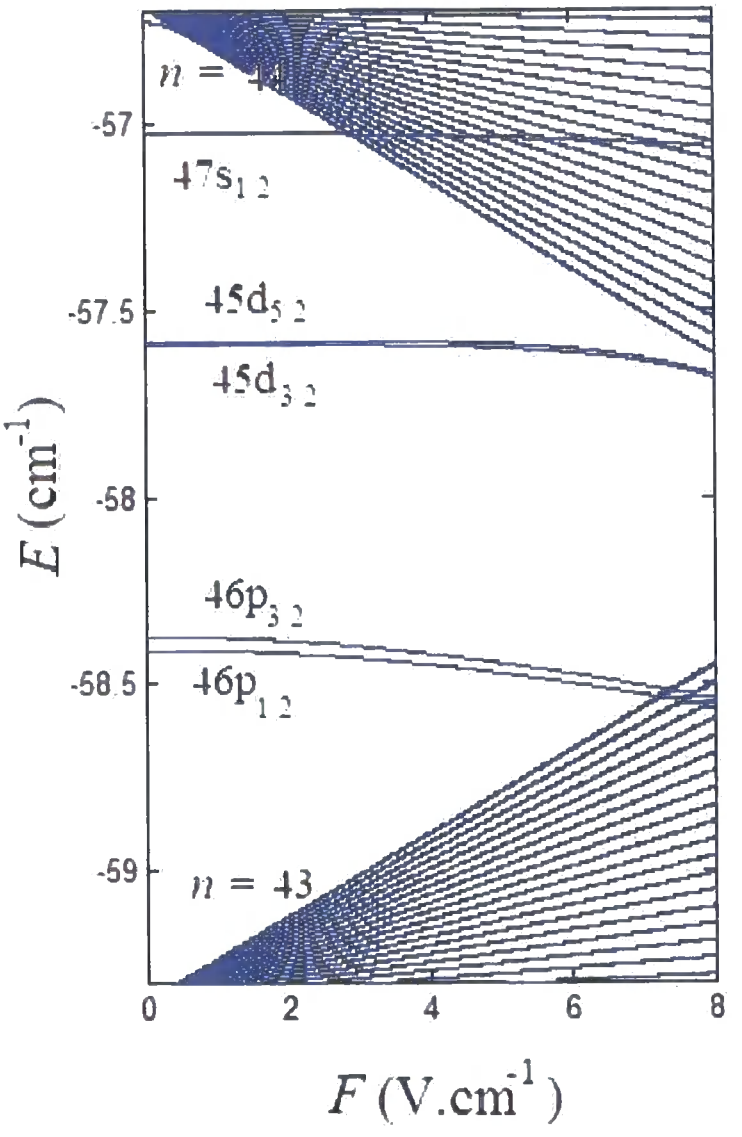

Figure 3.6: Electric field dependent energy levels around 45d state for $|m_j|$ = 0.5 calculated by diagonalization.

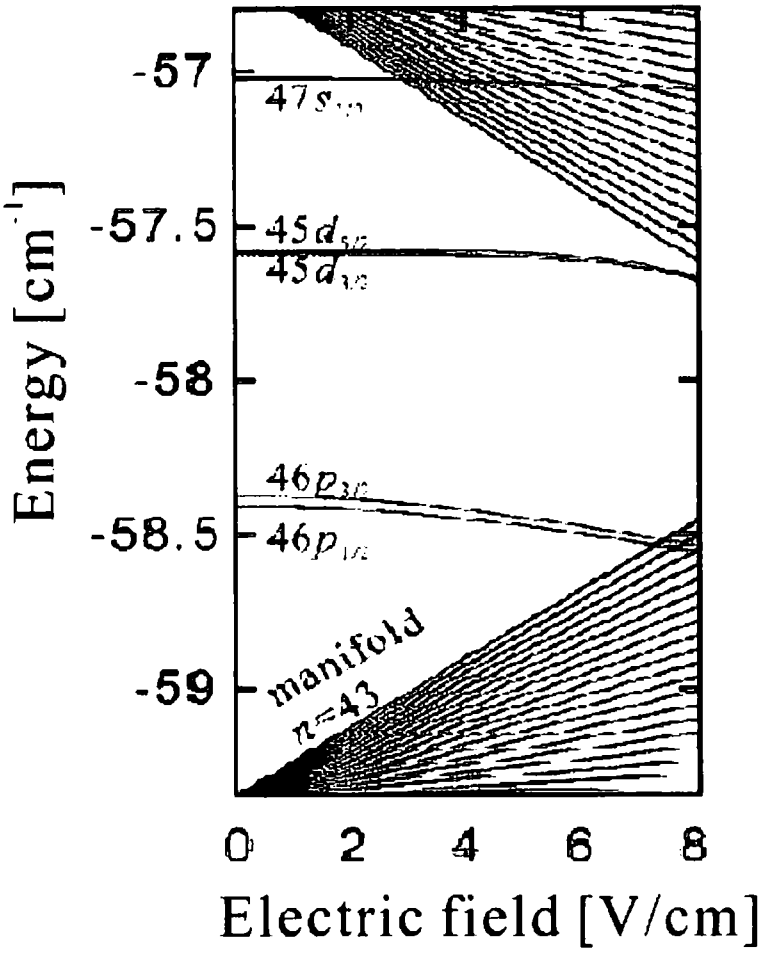

Figure 3.7: Electric field dependent energy levels around 45d state for $|m_j|$ = 0.5 calculated in [31].

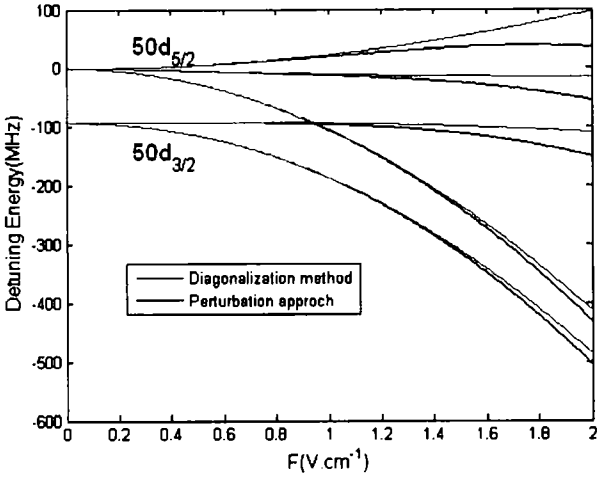

Figure 3.8: A demonstration of the Stark shifts of 50d states calculated using f-states and p-states by perturbation theory approaches(black) and diagonalization method(blue).

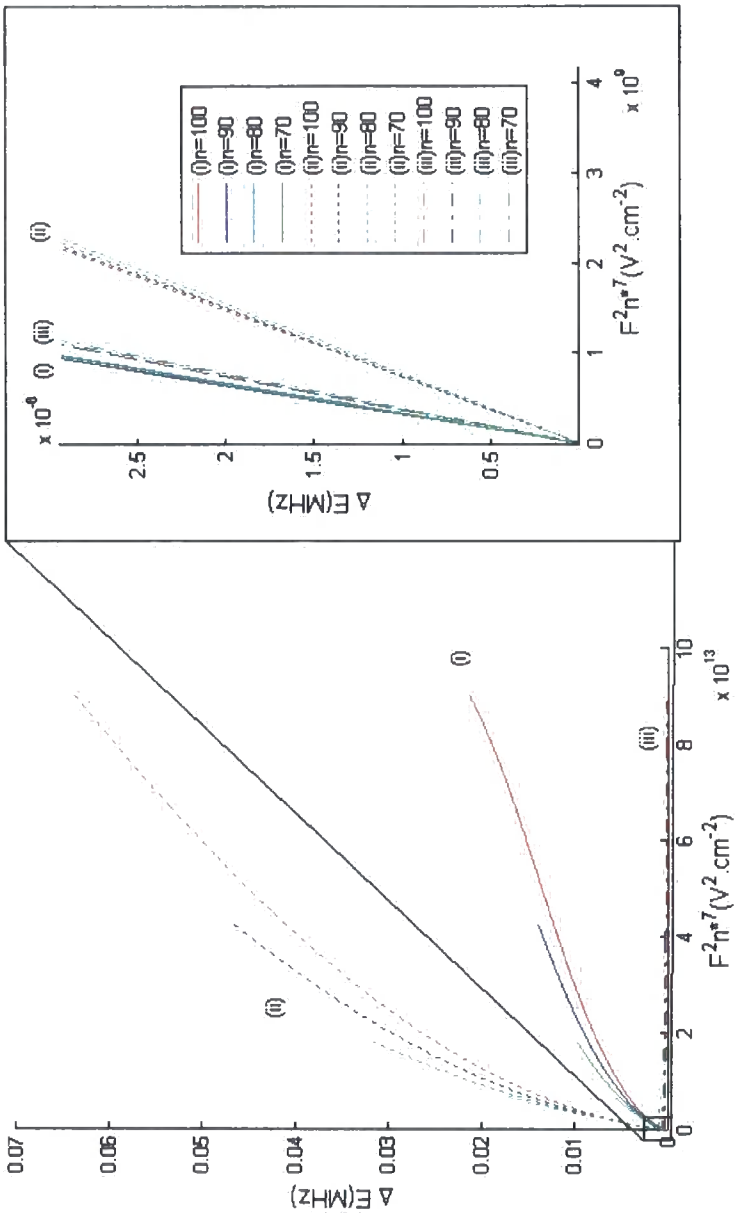

Figure 3.9: Scaled Stark shifts using scale transformation $F^{*2} = n^{*7}F^2$ of $(i)|E(n, l = 2, j = 3/2, m_j = 1/2) - E(n, l = 2, j = 3/2, m_j = 3/2)|$(solid lines) , $(ii)|E(n, l = 2, j = 5/2, m_j = 1/2) - E(n, l = 2, j = 5/2, m_j = 3/2)|$ (dash lines), $(iii)|E(n, l = 2, j = 5/2, m_j = 3/2) - E(n, l = 2, j = 5/2, m_j = 5/2)|$ (dash-dot lines), which n=100(red), 90 (blue), 80(cyan), 70(green).

Chapter 4

Stark splitting comparison with experiment

In this chapter we verify the results of our numerical calculation by comparing the calculated Stark shifts with real experimental results obtain in Stuttgart[36] which investigated Stark splitting of cold Rubidium atoms using laser excitation and field ionization. Subsequently, we compare the calculated spectra with experimented spectra using thermal atoms in vapour cell in Durham[35]. We show that the Durham results are more difficult to interpret due to the presence of ion in the vapour cell.

4.1 Comparison with Stuttgart experiments

In Stuttgart experiment[36], an applied field is applied to Rubidium atoms in a magneto optical trap (MOT). Then, the Rubidium atoms are excited by two lasers. Firstly, they are excited from $5S_{1/2}(F = 2)$ to $5P_{3/2}(F = 3)$ by a red laser with wave length 780.248 nm. Secondly, the atoms in $5P_{3/2}(F = 3)$ are excited to Rydberg state by blue laser with wave length 480.6 nm. In this experiment, the blue laser can be adjusted for the Rubidium transition from $5P_{3/2}(F = 3)$ to Rydberg states by accusto-optical modulator (AOM). Because of the master-slave laser system, the red laser is used as master laser and stabilized in resonance cavity to make the blue laser stable and adjustable in the order of 1 MHz. Consequently, the high resolution spec-

troscopy is obtained from this system and the Rubidium atoms are excited to Rydberg states more accurately. Based on field ionization, the Rydberg atoms is detected by applying pulsed electric field. Additionally, the amount of emerging ions is counted by micro channel plate (MCP). As shown in figure 4.1, the calculated results strongly agree with experimental results. Nevertheless, this comparison is emphasized on the reliability of diagonalization and Coulomb approximation.

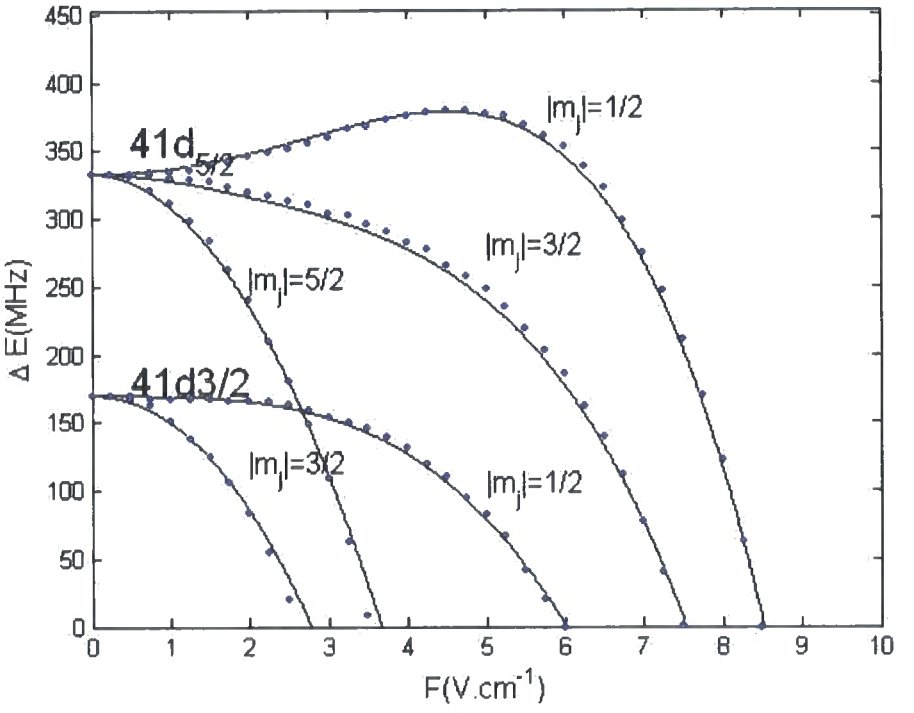

Figure 4.1: Comparison of electric field dependence energy levels of $41d_{3/2}$ and $41d_{5/2}$ between the Stuttgart experiment[36] (dot) and theoretical calculation (solid lines) with $|m_j|$= 0.5, 1.5 and 2.5.

4.2 The Durham Electromagnetically Induced Transparency(EIT) experiment

The EIT experiment is done by using two laser beams transmit through room temperature vapor chamber of Rubidium as be showed by figure 4.3 and 4.2. The first propagated laser called probe beam is fixed at 780 nm following transitions of $5s^2S_{1/2}(F = 3) \rightarrow 5p^2P_{3/2}$. The second beam called coupling beam is transmitted in the opposite direction to probe beam. The coupling beam is varied from 479 to 484 nm. This range of frequency can cover the transitions of $5p^2P_{3/2} \rightarrow nd^2D_{3/2,5/2}$ for $n = 26 - 124$. A photodiode is applied to measure the probe transmission measurement of the probe laser. As in figure 4.4, the result from transmission measurement of probe laser is is a function of coupling laser detuning. As shown in this figure, the transmission is a function of detuning of $44D_{5/2}$. The $44D_{5/2}$ and $44D_{3/2}$ states are evidently depicted in the region of the scanned coupling frequency on this graph.

In order to investigate the influence of the external electric field to spectrum of Rubidium, the vapour chamber is placed between two electrodes which apply an electric field controlled by rectifier with frequency 90 MHz (figure 4.6b). The experiment is done by varying the applied rf voltage which we obtain expected amplitude of rf electric field of the vapour chamber since the separation between electrodes is 3 cm. in table 4.2. Oscillating electric field is applied to the vapour following the presence of ions in the vapour cell. The cause of ions production could be photoionization by the applied laser fields[41]. Furthermore, by the reason that this experiment is done in room temperature, ions could be possibly produced by ionization in a thermal field which can raise collision rate and radiative transition[43][44]. It was found that this black body ionization depends on temperature and the large dipole transitions of Rydberg atoms[42]. The ions are also slightly produced by interactions between atoms which the production rate depends on density of the vapour by Li et al.[40]. Nevertheless, Li et al. have reported the significance ionization by atomic interaction in laser cooling trapped atoms which much denser than thermal atoms.

Table 4.1: Peak-to-peak voltages(V_p) applied to electrodes in EIT spectroscopy experiment[35] and corresponding peak-to-peak amplitudes of external electric field($F(p)$). The time dependent function of external electric field is described by function $F_{ext}(t) = (F_p/2)\sin(\omega t)$, which ω is angular frequency of applied voltage.

$V_p(mV)$	$F_p(\mathrm{V}.cm^{-1})$
480	0.080
760	0.127
1080	0.180
1480	0.247
1900	0.317
2380	0.397
2840	0.473
3340	0.557

As a result of the occurrence of ions in the vapour cell, ionic distribution is expected to compensate the external dc electric fields exactly, whereas the ions are harder to responds this compensation rapidly enough for the external ac electric fields.

4.3 Comparison results and results analysis.

After investigating experimental data in each peak-to-peak voltage in table 4.2, and by the ideal situation that the electric field seen by vapor Rubidium atoms is described by function $F_{eff} = F_{ext} = (F_p/2)\sin(\omega t)$, where F_{ext} is peak-to-peak external electric field we obtain comparison results between experiments and theoretical prediction in figure 4.5. The results in figure4.5 show inconsistency between the presumption of $F_{eff} = F_{ext}$ calculated and experimental results. The atoms see stronger field than external electric field considering from the slower shifts of the calculated results. However, since ions production in the vapour chambers was reported in Li et al.[40] and Potvliege and Adams[41] by various reasons, we have another expectation

including the influence of ionic dynamics in sufficient high electric fields. This presumption can be described by figure 4.6, where $F_{max} = F_p/2$. If very low frequency oscillating voltage is applied to the chamber, ionic charge distribution can be expected following compensation of the applied electric field. This certainly causes electric field cancellation in the chamber. Since frequency of oscillator in this experiment is designed in order to avoid this cancellated field by using efficient high frequency (90MHz), the eventually effect by ions with long relaxation time could be seen by this comparison results.

Referring to figure 4.6, if it is assumed that the initial charge distribution corresponds to the external electric field as figure 4.6b at $t = t_1 = 0$ as cancellation in figure 4.6a, the eventually charge distribution will change slightly at $t = t_2 = T$, where T is period of oscillation according to long relaxation time of the ions. We are able anticipate the subsequent cancellation and at t_1 and addition at t_2 in figure 4.6c and equation

$$\begin{aligned} F_{eff} = F_{int} + F_{ext} &= \frac{F_p}{2} + \frac{F_p}{2}\sin(\omega t) \\ &= \frac{F_p}{2} + \frac{F_p}{2}\sin(2\pi t/T), \end{aligned} \tag{4.1}$$

where F_{int} is electric field produced by screened charges. Independent to the form of equation (4.1), the calculation using equation (2.20) need only the maximum external field of equation (4.1) which is F_p and F_{eff} is expected to be F_{eff} exactly.

On the contrary, the more calculations are done in order to find the best fitting comparison by changing proportion of the effective field to the external field amplitude and we can observe higher effective field than the last assumption. The best fitting result is the calculation using $F_{eff} = 1.35F_{ext}$ which can be seen by figure 4.7.

In conclusion, we can evaluate the maximum effective electric field relating to peak-to-peak of oscillating electric field by a scale of 1/1.35 using best fitting calculated results into experimental results, whereas it is expected to be one regarding ideal slowly response charge.

At the same time we have done other theoretical predictions which can explain some model of the effective field corresponding to the comparison re-

sults. Because of the time dependent external field, the transmission as detuning in the experiments is the average transmission following the function of the external field.

Since each peak in the relation between transmission and detuning is the spontaneous emission from each energy level with significant life time (τ), using time dependent perturbation theory and N photons emitted from the energy states as a differential equation

$$\frac{dN}{dt} = -N\tau^{-1}, \tag{4.2}$$

the expected transmission(I) as a function of detuning(ω') is described by a proportion of the Lorentzian function[13][39]

$$I(\omega') = \frac{\tau^{-2}/4}{\omega'^2 + \tau^{-2}/4}. \tag{4.3}$$

The Lorentzian shape is showed in figure 4.8. Considering experimental results, not all peaks are symmetry and consistent with Lorentzian shape. This is found as an effect of the time dependent electric field on the photodiode detector. Using Lorentzian equation and calculated Stark shifts, we model the Stark shifts of nd states detected by EIT experiment without the influence of the oscillating electric field in figure 4.9. The blue lines corresponds to calculated Stark shifts in the black lines which separate from calculating when the oscillating field affects on the results in figure 4.10,4.11 modelled by $F_{eff} = (F_p/2)\sin(\omega t)$ and $F_{eff} = (F_p/4)(1 + \sin(\omega t))$, respectively.

Likewise, the modelling including time dependent is calculated by averaging transmission of the electric field described by a function of $F_{eff} \rightarrow F_{eff}(F_p, t)$, which is written as

$$S'(F_p, \omega') = \frac{\int_0^{t'} dt S(F_{eff}(F_p, t), \omega') dt}{\int_0^{t'} dt}, \tag{4.4}$$

where S is the transmission without the influence of time dependent electric fields as a function of the electric field and detuning at time t and S' is the transmission under the influence of time dependent electric fields. On the other hand, modelling of figure 4.9 which $F = F_p$ and is time-independence uses the function

$$S(F, \omega') = \sum_i I_i(\omega_i'(F), \omega'), \tag{4.5}$$

which

$$I_i(\omega_i'(F), \omega') = \frac{\tau^{-2}/4}{(\omega' - \omega_i'(F))^2 + \tau^{-2}/4}, \tag{4.6}$$

where i and ω_i' are index and detuning of each Stark shift, respectively. Since ω_i' is unable to be calculated analytically as a function of F and F_{eff} in equation (4.4) can be considered as a periodic function with period T and T is divided into small interval dt , the modelling by equation(4.4) is changed to discrete form

$$S'(F_p, \omega') = \frac{1}{N} \sum_{t=1}^{N} S(F_{eff}(F_p, t), \omega'), \tag{4.7}$$

where $N = T/dt$. The resonances observed in the experiment are clearly narrower than the resonance prediction by the sinusoidal modulation of the field which implies that the effect of the ions is to sharpen the switches time of the field. It follows that one of the distinctive separations between graphs on the basis of time dependent field influence is the shape and moderately distortion of peaks. The directions of the distortions in figure 4.9 depend on gradients of changing position of the peaks in figure 4.10 following increasing electric field oppositely, seeing that the transmission of the lower F_p have significant values to affect average transmission of the higher F_p. This modelling could also be taken advantage for comparison results between calculation and experiment as a criterion for crossing positions of calculated graph on the peaks of EIT experiments.

Besides, there are the addition peaks appears and constantly locate at the detuning energy of $44d_{3/2}$ and $44d_{5/2}$ in the zero field. One explanation of these appearances is the high intensity at both states in zero electric field and the more time the electric field spends in low field regime. The influence of time the electric field spends in low field region can be seen clearly from different strength between those inconsistent peaks with Stark shifts of figure 4.10 and 4.11, since the electric field in equation (4.1) spends more time in low field regime than the field $F_{eff} = (F_p/2)\sin(\omega t)$ as can be seen by figure 4.6b and 4.6c.

On the contrary, the inconsistent peaks are not visible in actual experimental results. This explains small time duration in low field regime. Accordingly, we improve a model of the effective electric field by criteria that ion distribu-

tion renders addition electric fields. The ions are assumed to partly behave as the screened charges compensate the applied field. As a result, the equation of the effective electric field is described by

$$F_{eff} = F_{max}\left[1 + \sin(\omega t) - A\sin(\omega t)\right], \tag{4.8}$$

where A is a phenomenological ratio of the screened field to the applied field which causes different shapes and time spending in low effective field (see figure 4.12). Subsequently, we model using A = 0.9 and 0.75 in figure 4.13 and 4.14, which the amount of screened responding to external electric field ions renders on shape and appearance of peaks. The appearance of peaks indicates time duration in the maximum and minimum electric fields which can be seen in the figure 4.12. For instance, there are two peaks obviously appear on both lines of d_j with $|m_j| = j$. The lower peaks are consistent with all previous models owing to expending time at the maximum field. Similarly, the minimum field in the figure 4.12 causes the upper peak indicated by correspondence to the positions of peaks at the minimum field before averaging inasmuch as equal duration in the maximum field. However, the fluctuation of the electric field still represents as shaping the peaks asymmetric. Comparing to the experiments using $F_p = 0.397, 0.473$, and 0.557, we can see the two splitting peaks similar to the last model in state $44d_{3/2}$ with $|m_j| = 3/2$ and it seem likely that the lower peaks rise, whereas the upper peaks reduce corresponding to the increasing electric field. The imbalance rising between the upper and lower peaks explain more phenomena cause this imbalance and the ratio A as a function of F_p which is unexplainable in this point. Comparing the figure 4.7, 4.13, and 4.14, we also found that the appearance of double peak in the experiment which the separation between peaks is short can be related to the model with low A which has shorter distance between peaks than the model with high A.

It seems like we come closer to the influence of actual ions dynamics. However, the last model suggests the lower F_{eff} since a larger A leads to F_{eff} converges toward $F_p/2$ or $F_{ext}/2$. Together with no partly screened charge compensated the applied field ($A = 0$) model, the range of the effective field is expected in between $F_p/2$ and F_p which is less than comparison results in figure 4.7 ($F_{eff} = 1.35F_p$). This means there are other addition fields cause addition F_{max} as a result of time dependence charge distribution. One

possible factor left is different motivities and cross sections between positive charges and negative which positive ions individually consists in nucleus and core electrons which are indoubtably heavier than negative charges which are sole ionized electrons. We can expect this heavier mass decelerates the positive charge movement and leads to more complex charge dynamics and unpredictable effective electric field.

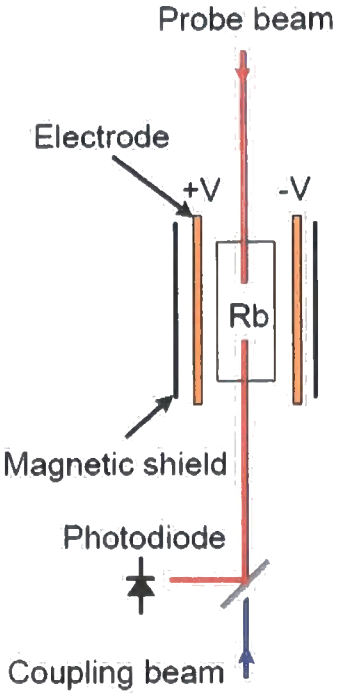

Figure 4.2: Experimental set-up of EIT by Mohapatra et al[35].The propagation of the probe laser and the coupling beam laser are set in opposite direction transmit through Rubidium vapor cell. The effect of coupling beam detuning between 479-484 nm on transmission of the probe beam is detected by photodiode and two parallel electrodes are introduced to the experimental set up in order to investigate influence of an electric field on Rubidium atoms.

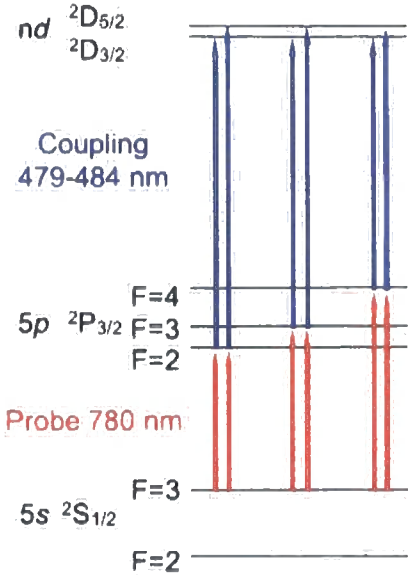

Figure 4.3: Diagram of energy level used by Mohapatra et al. [35]. Probe beam wavelength is set constantly at 780nm, which corresponds to $5s^2S_{1/2}(F = 3) \rightarrow 5p^2P_{3/2}$ transition(red), by the effect of effective wavelength of atoms with random velocity. Coupling beam wavelength is varies between 479-484 nm corresponding to $5p^2P_{3/2} \rightarrow nd^2D_{3/2,5/2}$ where $n = 26 - 124$(blue).

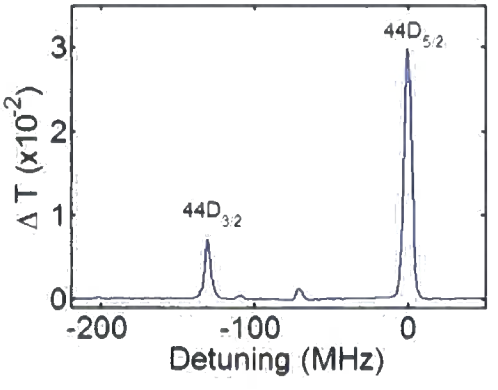

Figure 4.4: Transmission of probe laser as a function of detuning of coupling laser in the region of wavelength corresponding $5p^2P_{3/2} \rightarrow 44d^2D_{3/2,5/2}$ without applied external electric field.

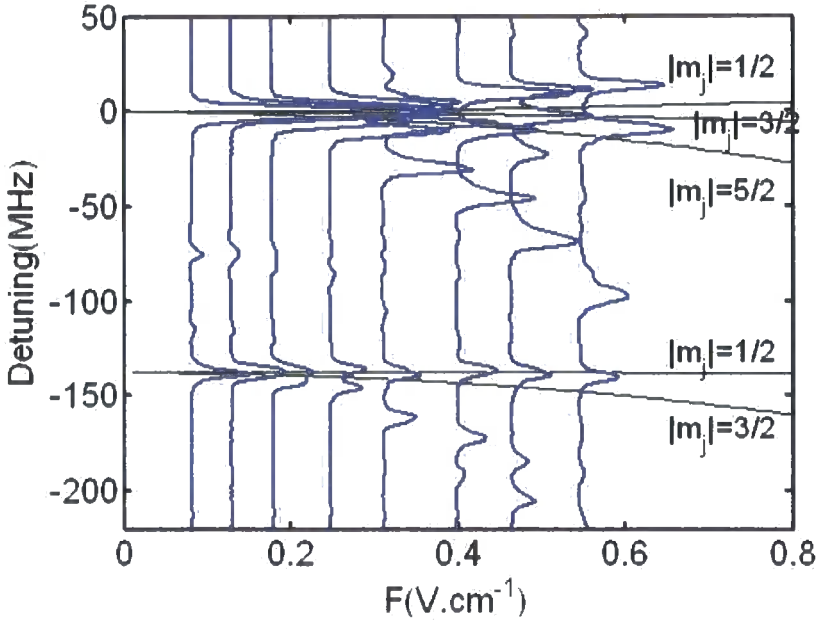

Figure 4.5: Stark shifts of $44d_{3/2}$ and $44d_{5/2}$ observed by EIT experiments(blue) and calculated results predicting effective electric field as functions of external electric field (F_{ext}) in black lines.

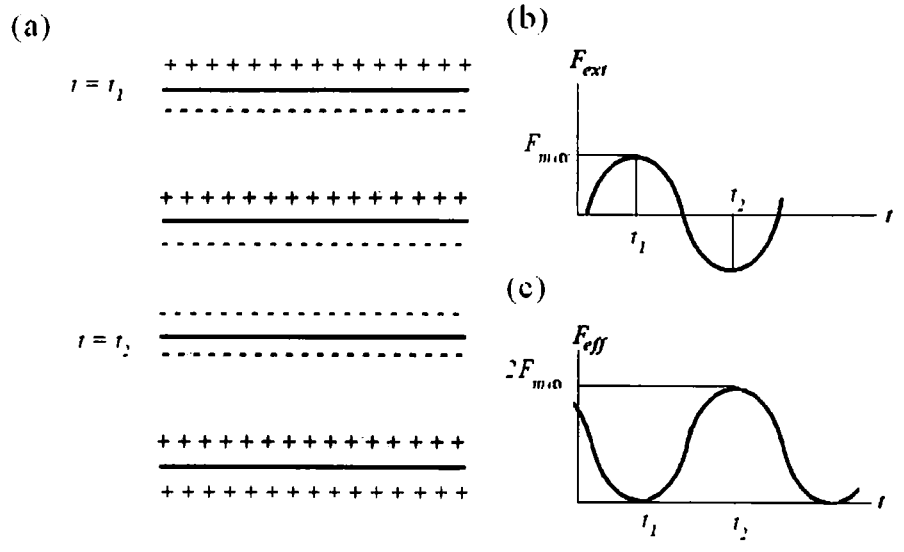

Figure 4.6: (a)Dynamics of Rubidium ions between electrodes corresponding to (b) sinusoidal external electric field with high frequency and (c) total electric field eventually affected by charge distribution of Rubidium ions.

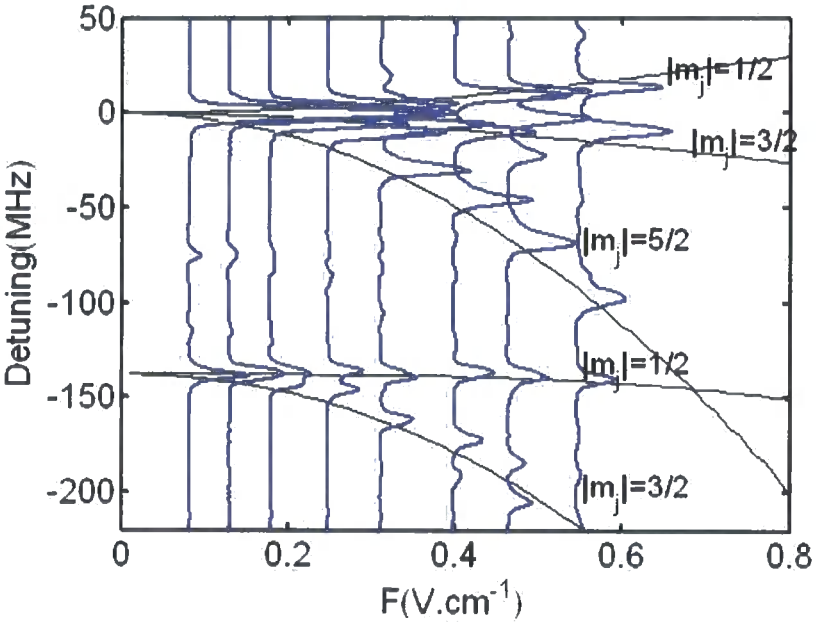

Figure 4.7: Stark shifts of $44d_{3/2}$ and $44d_{5/2}$ observed by EIT experiments(blue) and calculation results predicting effective electric field as functions of external electric field by using $F_{eff} = 1.35F_{ext}$(black).

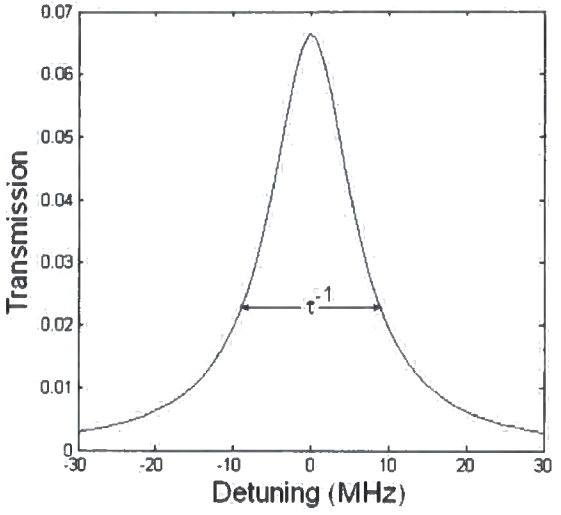

Figure 4.8: Lorenzian shape of transmission as a function of detuning described by equation (4.3).

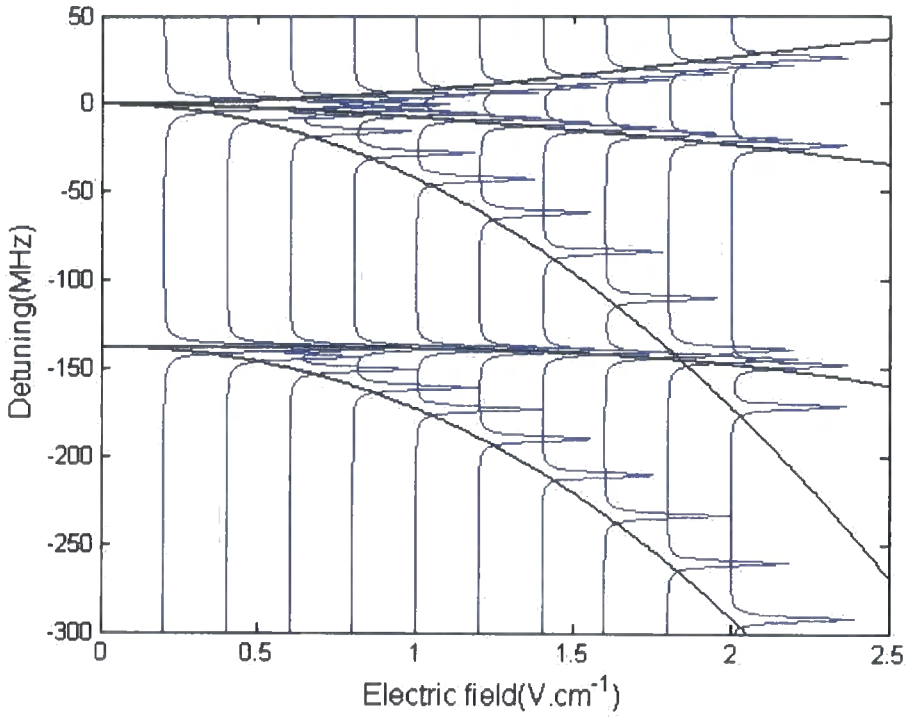

Figure 4.9: Modelling of Stark shifts of nd states by EIT experiments results without the influence of the oscillating electric field(blue) corresponding to calculated Stark shifts(black).

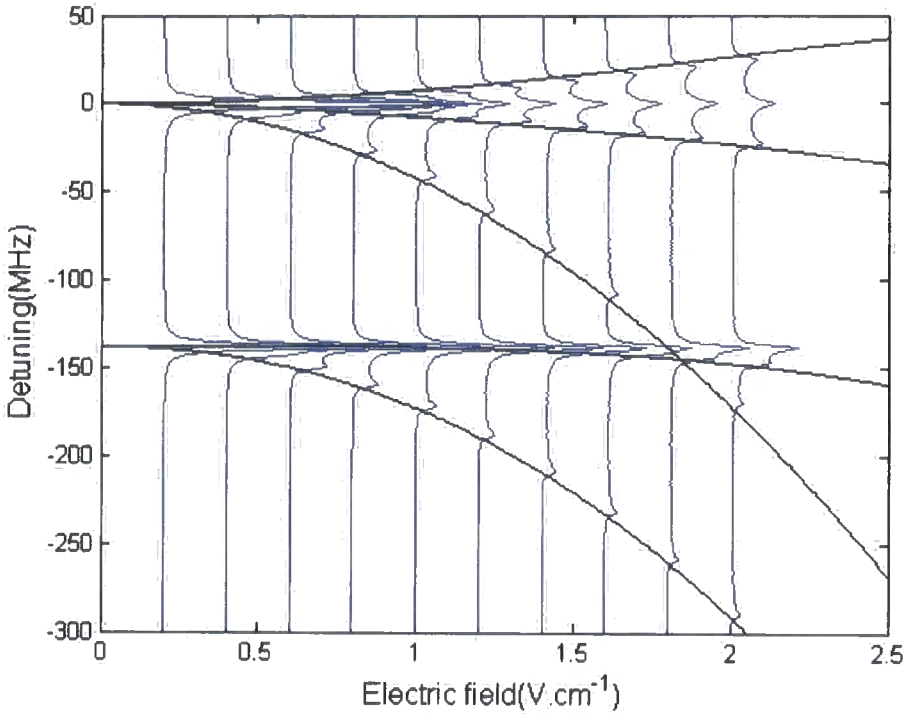

Figure 4.10: Modelling of Stark shifts of 44d states by EIT experiments results with the influence of the oscillating electric field(blue) $F_{eff} = F_{ext} = (F_p/2)\sin(\omega t)$ corresponding to calculated Stark shifts(black).

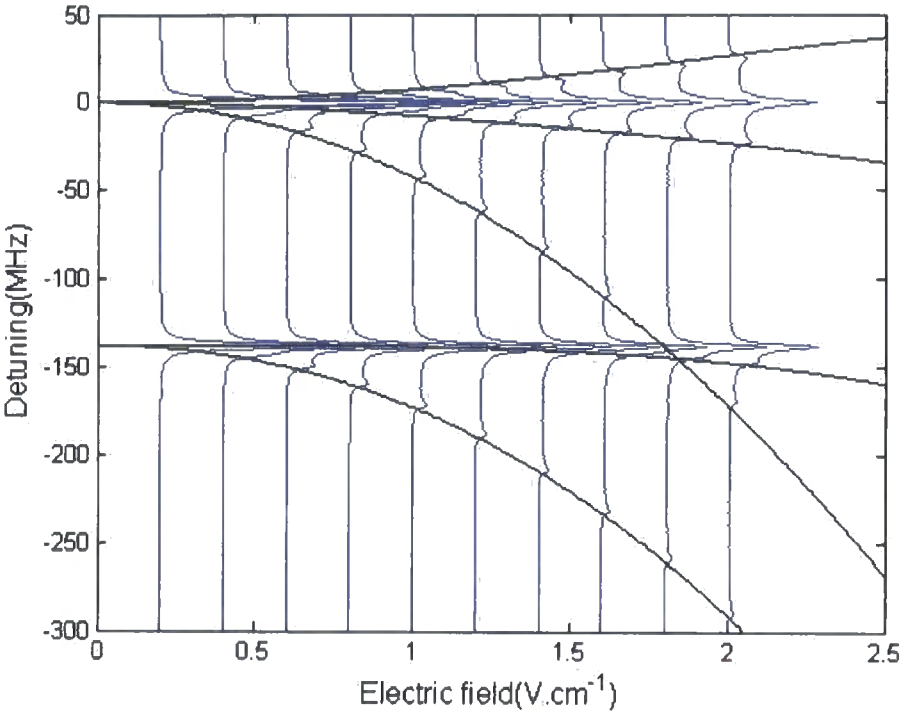

Figure 4.11: Modelling of Stark shifts of 44d states by EIT experiments results with the influence of the oscillating electric field(blue) $F_{eff} = (F_p/4)(1+\sin(\omega t))$ corresponding to calculated Stark shifts(black).

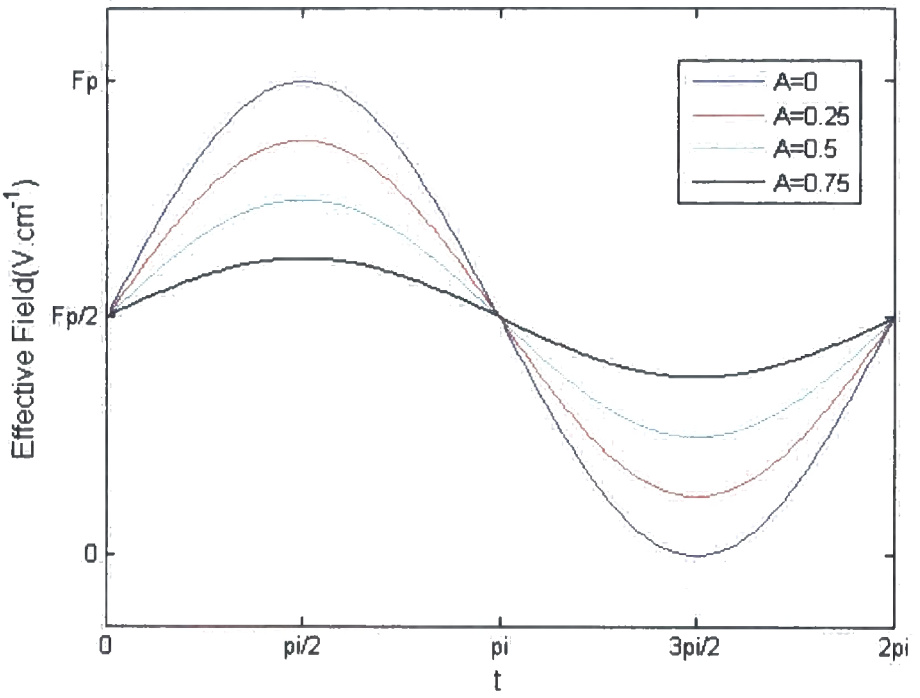

Figure 4.12: Effective field in different values of the ratio of the screened field by external field responsive ions to the applied field.

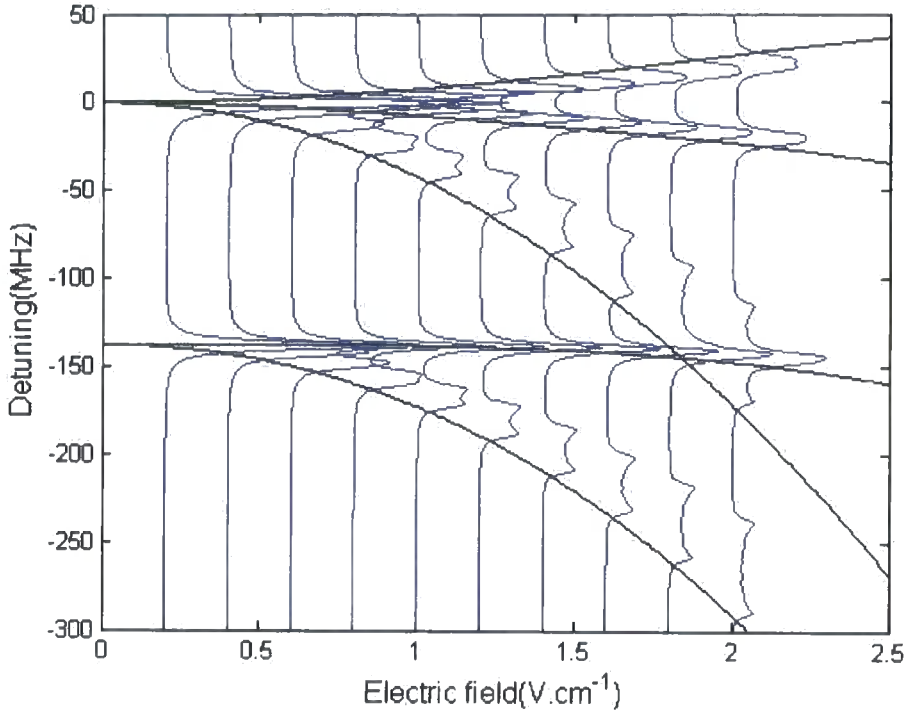

Figure 4.13: Modelling of Stark shifts of nd states by EIT experiments results with the influence of the oscillating electric field(blue) $F_{eff} = F_{max}\,[1 + \sin(\omega t) - A\sin(\omega t)]$ with $A = 0.9$ corresponding to calculated Stark shifts(black).

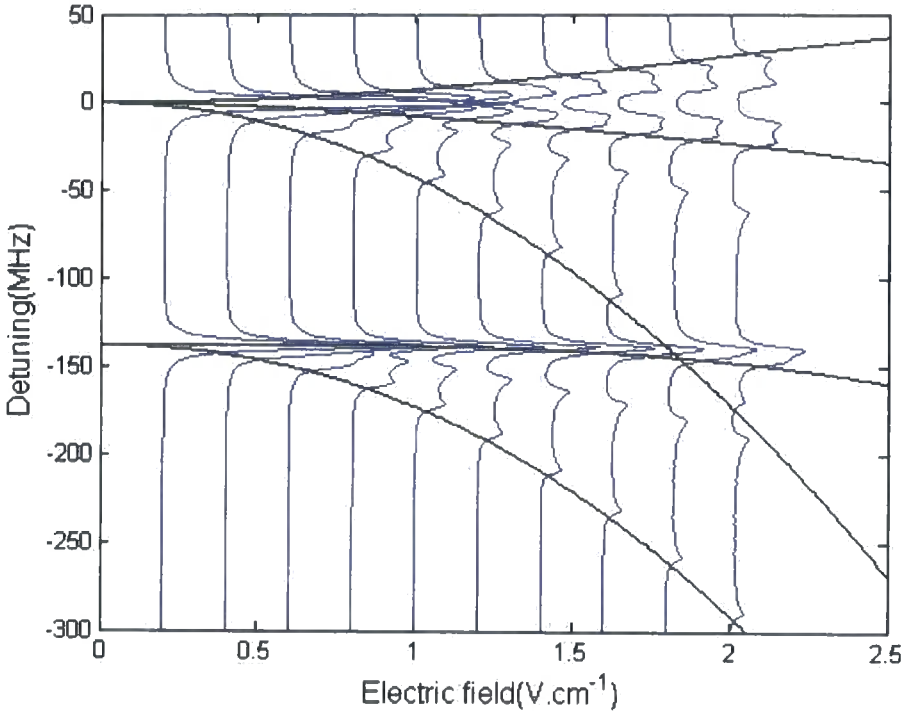

Figure 4.14: Modelling of Stark shifts of 44d states by EIT experiments results with the influence of the oscillating electric field(blue) $F_{eff} = F_{max}\left[1 + \sin(\omega t) - A\sin(\omega t)\right]$ with $A = 0.75$ corresponding to calculated Stark shifts(black).

Chapter 5

Conclusion

In summary, the conclusion is roughly divided into two parts,the spectra prediction in the electric field using diagonalization and comparison study with EIT experiments.

Following the numerical tests and comparison with Stark shifts detection done in Stuttgart, both non-relativistic and hyperfine splitting Stark shifts can be predicted efficiently using diagonalization together with radial integral calculated by Coulomb approximation. Along with diagonalization calculation, Stark shifts calculation of very high n can be generalized by scaling law of n^7 in very low electric fields.

In the part of comparison with EIT experiments, it is found that because of representation of ions in the vapour chamber the time average spectrum is sensitive to a dc effect of the applied field. It is possible that this offset may depend on the amplitude of all applied field and may even depend on the previous history of applied fields making exact spectra difficult to reproduce by EIT. Further experimental work is require to produce an exact quantitative comparison with theoretical spectra.

Bibliography

[1] Mourachko I, Comparat D, de Tomasi F, Fioretti A, Nosbaum P,Akulin V M and Pillet P 1998 *Phys. Rev. Lett.* **80** 253.

[2] Anderson W R,Veale J R and Gallagher T F 1998 *Phys. Rev. Lett.* **80** 249.

[3] Carroll T J,Claringbould K, Goodsell A, Lim M J and Noel M W 2004 *Phys. Rev. Lett.* **93** 15300

[4] Carroll T J, Sunder S and Noel M W 2006 *Phys. Rev. A* **73** 032725

[5] Jaksch D,Cirac J I,Zoller P,Rolston S L, Cote R and Lukin D 2000 *Phys. Rev. Lett.* **85** 2208

[6] Gallagher T F 1992 *Phys. Rep.* **210** 319

[7] Rauschenbeutel A, Nogues G, Osnaghi S, Bertet P, Brune M, Raimond J M and Haroche S 1999 *Phys. Rev. Lett.* **83** 5165

[8] Protsenko I E, Reymond G, Schlosser N and Grangier P 2002 *Phys. Rev. A* **65** 052301

[9] Lukin M D, Fleischhauer M, Côté R, Duan L M Jaksch D Cirac J I and Zoller P 2001 *Phys. Rev. Lett.* **87** 037901

[10] Tong D, Farooqi S M, Stanojevic J, Krishnan S, Zhang Y P, Côtée R, Eyler E E and Gould P L 2004 *Phys. Rev. Lett.* **93** 063001

[11] Marinescu M 1997 *Phys. Rev. A* **56** 4764

[12] Gallagher T F *Rydberg Atoms* Cambridge University Press, Cambridge 1994

[13] Bransden B H and Joachain C J *Physics of Atoms and Molecules* Pearson Educational Limited, Essex 2003

[14] Bethe H A and Salpeter E A *Quantum Mechanics of One and Two Electron Atoms* Academic Press, New York 1957

[15] Seaton M J 1983 *Rep. Prog. Phys.* **46** 167

[16] Hartree D R 1928 *Roc. Camb. Phil. Soc.* **24** 426

[17] Burgess A and Seaton M J 1960 *Mon. Not. R. Astron. Soc.* **120** 121

[18] Klapisch M 1967 *C. R. Acad. Sci. Ser. B* **265** 914

[19] Whittaker E T and Watson G N *A course of modern analysis* Cambridge University Press, London 1927

[20] Gordon W 1929 *Ann. Phys.* **2** 1031

[21] Bates D R and Damgard A 1949 *Phil. Trans. R. Soc. A* **242** 101

[22] van Regemertor H, Hoang Bihn Dy and Prud'homme M 1979 *J. Phys. B.* **12** 1053

[23] Klarsfeld S 1989 *Phys. Rev. A.* **39** 2324

[24] Hylleraas E A 1946 *Arch. Math. Naturv.* **48** 57

[25] Potvliege R 1998 *Comput. Phys. Commun.* **114** 42

[26] Zimmerman M L, Littman M G, Kash M M and Kleppner D 1979 *Phys. Rev. A* **20** 2251

[27] Picart J, Edmonds A R, and Tran Minh N 1978 *J. Phys. B :Atom. Molec. Phys.* **11** L651

[28] Edmonds A R, Picart J, Tran Minh N and Pullen R 1979 *J. Phys. B :Atom. Molec. Phys.* **12** 2781

[29] Naccaceh N P 1972 *J. Phys. B. :Atom. Molec. Phys.* **5** 1308

[30] Abramowitz M and Stegun I A *Handbook of Mathematical Functions* Courier Dover Publications, Washington DC 1965

[31] Haseyama T, Kominato K, Shibata M, Yamada S, Saida T, Nakura T, Kishimoto Y, Tada M, Ogawa I, Funahashi H, Yamamoto K and Matsuki S 2003 *Phys. Lett. A* **317** 450

[32] Li W, Mourachko I, Noel M W and Gallagher T F 2003 *Phys. Rev. A* **67** 052502

[33] Sobelman I I *Atomic Spectra and Radiative Transitions* Springer-Verlag Berlin Heidelberg, New York 1979

[34] Gallagher T F 1988 *Rep. Prog. Phys.* **51** 143

[35] Mohapatra A K, Jackson T R and Adams C S 2007 *Phys. Rev. Lett.* **98** 113003

[36] Grabowski A, Heidemann R,Low R,Stuhler J and Pfau T 2006 *Fortschr. Phys.* **54** 765

[37] Davydkin A A, and Zon B A 1981 *Opt. Spectrosc. (USSR)* **51** 13

[38] Kishimoto Y 2002 *Mem. Fac. Sci. Kyoto Univ. ,Ser. Phys.* **38** 163

[39] Fleischhauer M, Imamoglu A and Marangos J P 2005 . *Rev. Mod. Phys.***77** 633

[40] Li W, Tanner P J and Gallager T F 2005 . *Phys. Rev. Lett.***94** 173001

[41] Potvliege R M and Adams C S 2006 . *New J. Phys.***8** 163

[42] Spencer W P, Vaidyanathan A G, Kleppner D and Ducas T W 1982 . *Phys. Rev. A***26** 1490

[43] Beiting E J, Hildebrandt G F, Kellert F G, Foltz G W, Smith K A, Dunning F B and Stebbings R F 1979 . *J. Chem. Phys.***70** 355

[44] Hildebrandt G F, Beiting E J, Higgs C, Hatton G J, Smith K A, Dunning F B and Stebbings R F 1981 . *Phys. Rev. A***23** 2978